Upward delamination of Cascadia Basin sediment infill with landward frontal accretion thrusting caused by rapid glacial age material flux

Juergen Adam,[1,2] Dirk Klaeschen,[3] Nina Kukowski,[1] and Ernst Flueh[3]

Received 1 November 2002; revised 10 March 2004; accepted 31 March 2004; published 26 June 2004.

[1] The Cascadia convergent margin is a first-order research target to study the impact of rapid sedimentation processes on the mechanics of frontal subduction zone accretion. The near-trench part of the accretionary prism offshore Washington is affected by strongly increased glacial age sedimentation and fan formation that led to an outstanding Quaternary growth rate with landward vergent thrust faulting that is rarely observed elsewhere in accretionary wedges. Multichannel seismic reflection data acquired on the ORWELL project allows us to study the structure and dynamics of the atypical frontal accretion processes. We performed a kinematical and mechanical analysis of the frontal accretion structures, and developed a dynamic Coulomb-wedge model for the landward-verging backthrust formation. Backthrusting results from heterogeneous diffuse strain accumulation in the mechanically heterogeneous Cascadia basin sediment succession entering the subduction zone, and strain partitioning along a midlevel detachment that is activated by gravitational loading caused by rapid glacial age sedimentation. These complex deformation processes cause the passive "upward" delamination of the upper turbidite beds from the basal pelagic carbonate section similar to triangle-zone formation and passive backthrust wedging in foreland thrust belts caused by rapid burial beneath syntectonic sediment deposits. The deformation mechanism at the tectonic front of the Cascadia margin is an immediate response to the strongly increased late Pleistocene sediment flux rather than to atypical physical boundary conditions as generally thought. *INDEX TERMS:* 8105 Tectonophysics: Continental margins and sedimentary basins (1212); 8110 Tectonophysics: Continental tectonics—general (0905); 8122 Tectonophysics: Dynamics, gravity and tectonics; 8150 Tectonophysics: Plate boundary—general (3040); *KEYWORDS:* accretionary wedge, subduction zone, active tectonics, fault mechanics, exogenetic processes, triangle zone. **Citation:** Adam, J., D. Klaeschen, N. Kukowski, and E. Flueh (2004), Upward delamination of Cascadia Basin sediment infill with landward frontal accretion thrusting caused by rapid glacial age material flux, *Tectonics*, *23*, TC3009, doi:10.1029/2002TC001475.

1. Introduction

[2] Whereas it is commonly accepted that climate-driven flux of sediment to the offshore part of the continental margin governs the width and growth rates of accretionary prisms, its possible control of the mechanics of subduction accretion has not been addressed so far. The Cascadia margin is a first-order location to study the influence of climate-driven mass-transfer on the mechanics of tectonic accretion at active margins. The structural style, growth rate, and the accretion mechanism of the fast-growing Quaternary Cascadia accretionary complex (Figure 1) vary significantly along-strike reflecting the increased and highly variable glacial age sediment flux to the Cascadia Basin [*Calvert*, 1996; *Davis and Hyndman*, 1989; *MacKay*, 1995; *MacKay et al.*, 1995; *Niem et al.*, 1992; *Seely*, 1977; *Snavely*, 1987].

[3] In the accretionary prism at the base of the more narrow continental slopes off Vancouver Island [*Hyndman et al.*, 1995] and central Oregon south of 45°N [*MacKay*, 1995] seaward vergent thrust faults typical for submarine accretionary wedges were identified. In contrast, along the central broadened continental slope off Washington [*Flueh et al.*, 1998] and northern Oregon [*MacKay*, 1995], landward vergent thrust faults in the frontal prism reveal a rather atypical accretionary style.

[4] The regional extend of the landward vergent thrusts correlates with those segments of the deformation front bordering the Nitinat fan and parts of the Astoria abyssal fan. These large deep see fans consist of continentally derived turbidite deposits resulting from increased glacial age sediment input from the Frazier and Columbia Rivers, respectively [*Applegate et al.*, 1992; *O'Connor and Baker*, 1992; *O'Connor et al.*, 1995]. Because the arcward Pre-Quaternary to Miocene part of the accretionary wedge beneath the upper slope is affected by seaward-vergent thrusts as documented by wide-angle and MCS reflection seismic data [*Fisher et al.*, 1999; *Flueh et al.*, 1998], it was proposed that the major change of the style of accretion occurred simultaneously with the onset of glacial age sedimentation of the fan deposits [*Fisher et al.*, 1999; *Flueh et al.*, 1998].

[1] GeoForschungsZentrum Potsdam, Potsdam, Germany.
[2] Now at the Department of Earth Sciences, Dalhousie University, Halifax, Nova Scotia, Canada.
[3] GEOMAR, Forschungszentrum für Marine Geowissenschaften der Christian-Albrechts-Universität zu Kiel, Kiel, Germany.

0278-7407/04/2002TC001475$12.00

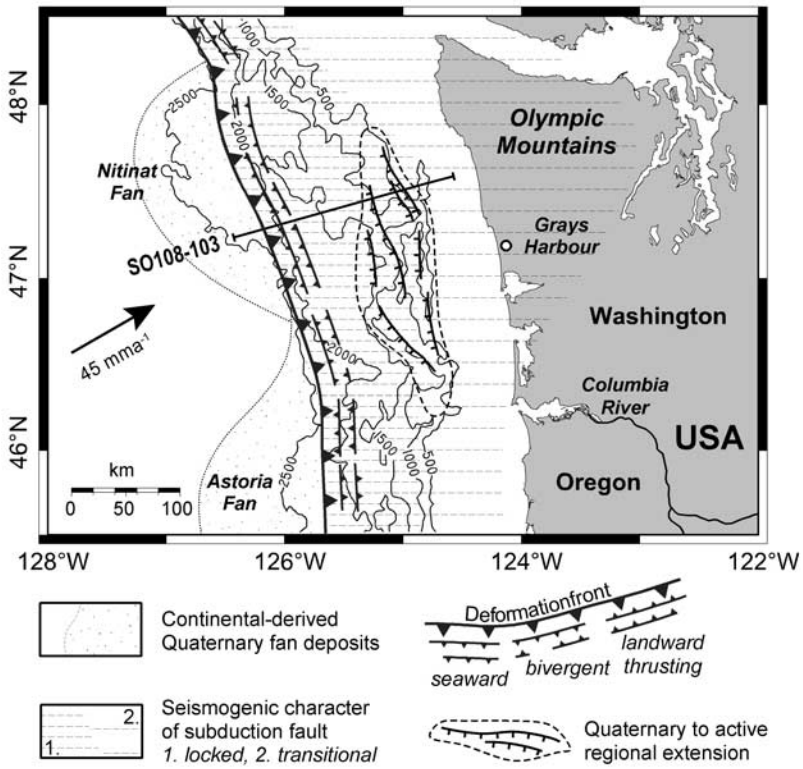

Figure 1. Tectonic features of the Cascadia convergent margin with location of the MCS profile SO108-103 of the ORWELL experiment [*Flueh et al.*, 1998]. Thrust fault signature indicates structural vergence of frontal accretionary structures. Normal faults at the shelf edge indicate a region of Quaternary to active extension [after *McNeill et al.*, 1997]. Seismogenic character of Cascadia subduction fault as derived from GPS data [*Khazaradze et al.*, 1999].

[5] This obvious correlation raises the question whether sedimentary mass transfer has the potential to efficiently and promptly reorganize fault mechanics in accretionary wedges. Particularly for Cascadia, a conclusive explanation for the atypical accretion mechanism and its controlling factors is of fundamental importance because this convergent margin is thought to have a huge potential for the nucleation of very large subduction zone earthquakes. A wealth of palaeoseismological data, e.g., tsunami deposits along the Oregon and Washington coast [*Clague*, 1997] and tsunami records of a large Cascadia event at the Japanese coast [*Satake et al.*, 1996] give evidence for large subduction earthquakes of magnitude 8 with an inferred recurrence interval of several hundred years in the offshore segment of the subduction zone. However, because of the lack of large earthquakes in (US-) historical time, little is known about source locations and mechanisms of Cascadia subduction earthquakes. Therefore analysis of the kinematics and mechanics of Quaternary deformation processes in the accretionary complex contributes new information and thinking about the neotectonic and seismotectonic behavior of the Cascadia margin. On the basis of geodetic data [*Khazaradze et al.*, 1999] and thermal modeling [*Oleskevich et al.*, 1999], the complete offshore subduction interface from the trench down-dip to beneath the coast is placed within the seismogenic locked zone (Figure 1).

[6] It is the aim of this study that include the presentation of a re-processed seismic section, seismic attributes, structural balancing, and frictional wedge analysis to study the mechanics of landward vergent thrusts and its response to rapid sedimentation. This also provides new understandings of the mechanism and source regions for potential earthquakes at the up-dip limit of the Cascadia seismogenic zone.

2. Previous Mechanical Concepts

[7] Previously published mechanical concepts for the unusual accretion mechanism by dominant landward vergent thrusting off Washington and northern Oregon invoked atypical physical boundary conditions, a non-Coulomb rheological approach or complex backstop/subduction geometries. *Seely* [1977] proposed that landward vergence along the Washington margin was primarily the result of low basal shear stress due to rapid deposition of trench sediment succession and related overpressuring. Also, *Byrne et al.* [1993] note that basal friction is the primary control on vergence and that low basal shear stress is essential for the development of landward vergence. *MacKay* [1995] emphasized that solely low basal shear stresses lead to the formation of conjugate thrusts and mixed-vergent structures, and in addition an arcward dipping décollement and a mechanically strong wedge with

respect to its base is required to favor dominantly landward vergent thrusts.

[8] *Gutscher et al.* [2001] discussed the mechanics of landward vergence in relation to a non-Coulomb, viscoelastic deformation behavior in the basal carbonate sequence of the Cascadia Basin sedimentary succession and to rapid loading due to the propagating Nitinat and Astoria deep-sea fans, and showed that analogue sandbox models with a ductile basal layer consisting of silicone putty were capable to produce an array of trenchward-propagating landward vergent thrusts.

[9] The occurrence of backthrusts as a consequence of sediment overthrusting onto a rigid seaward tapering rigid backstop in addition to the thermal history of the Cascadia subduction zone was discussed by *Byrne and Hibbard* [1987]. *Storti et al.* [2000] showed in a series of sandbox experiments and analytical analysis simulating a doubly-vergent thrust wedges (e.g., collisional orogens and collisional arcs) that backthrusts are common to develop in early-stage deformation above a velocity singularity.

3. Regional Tectonic Setting and Structural Position of Seismic Section

[10] At the Cascadia margin, the young (4–8 Myr) oceanic Juan de Fuca plate subducts beneath the North American continent at a moderate convergence rate of 45 km/m.y. and a shallow subduction angle increasing from 2° near the trench to 12° beneath the onshore part [*DeMets et al.*, 1990; *Engebretson et al.*, 1983; *Flueh et al.*, 1998; *Kulm et al.*, 1984] (Figure 1).

[11] Across the significantly broadened continental slope offshore Washington, marine reflection seismic data acquired during the 1996 "Orwell" project [*Fisher et al.*, 1999; *Flueh et al.*, 1997, 1998] reveal widespread active landward vergent thrusts in the frontal accretionary prism (Figure 2). Here, the Quaternary accretionary complex is characterized by a broad midslope terrace, bordered landward by seaward dipping listric normal faults of Miocene to Holocene age at the upper slope and the shelf edge (Figure 1) [*McNeill et al.*, 1997]. Rapid Quaternary frontal accretion, resulting from the accumulation of a thick sedimentary pile (about 3.5 km at 45°N [*Flueh et al.*, 1998] at the base of the slope, led to a seaward propagation of the deformation front of 30 to 50 km in the past 1.5 to 2 m.y. [*Barnard*, 1973].

[12] The 170-km-long MCS profile SO 108-103 [*Flueh et al.*, 1998] off the central Washington coast trends ENE-WSW normal to the deformation front (Figure 1) and extends from the undeformed Cascadia basin succession close to the shore (Figure 2). The seaward part of this profile, as presented in this study, transects the frontal accretionary prism (CMPs 1400 to 3000) and provides a high-resolution seismic image of the atypical landward vergent accretion structures (Figure 3a). The profile was processed applying iterative prestack-depth migration techniques together with velocity analysis from wide-angle OBH recordings to build an optimized depth section for structural balancing and kinematic analysis.

[13] The velocity structure of complexly deformed structures has an important impact on the resulting seismic image. Problems related to velocity variations that potentially cause fault shadows, pull-ups, and push-downs are only properly solved by prestack depth migration. Prestack depth migration can greatly improve imaging compared to normal time migration, because ray paths and their bending are accurately estimated trough the depth model, resulting in less distortions of the complex subsurface structure (correct reflector positions in depth) [see *Black and Brzostowski*, 1994]. Further, the depth migration resolves velocity information much better than time domain processing and estimates interval (rock) velocities which are independent of the reflector dip.

[14] The prestack depth migration algorithm applied to the ORWELL line in this study is the GX Technology Kirchhoff migration SIRIUS package, including common image gather and focusing analysis for velocity estimation. The estimation of the velocities during prestack depth migration is an iterative process based on the horizontal alignment of events in common image gathers. The residual curvature of the reflectors provides information on the adequacy of the migration velocity model. When the velocity used for the migration is incorrect, the imaging depth will be wrong. The focusing principle allows finding the depth where the stacking energy is at its maximum and calculates an improved estimate of the correct velocity [see *Guo and Fagin*, 2002]. By updating the velocities from top to bottom iteratively along the seismic profile a geological macro velocity model with the major tectonic structures was created. Great care was devoted to an accurate spatial imaging and the identification of the fold/thrust fault geometry, and secondary deformation structures at greater depths (e.g., basal part of the frontal accretionary wedge, top of the oceanic basement). The velocity analysis was performed at a spacing of 625 m and is precise up to 5% within the upper 2 km and between 5–10% within the 2–4 km range below the seafloor.

[15] The final velocity model includes the results from wide-angle OBH recordings, especially from the deep parts more than 4 km below the seafloor. Here the wide-angle data allow more precise velocity estimation because of the wide aperture of OBH recordings.

[16] The detailed final velocity model was further used to calculate seismic attributes to constrain physical properties (porosity, fluid accumulation, etc.) within the sedimentary pile. The exact relation between porosity and seismic velocity involves several unknowns, so we applied a non-linear empirical relationship between porosity and velocity on the basis of Arthy's law (see *von Huene et al.* [1998] for description of method and further references).

4. Seismic Stratigraphy and Prominent Structures

[17] In the seismic section (Figure 3a), sediment thickness increases from 2.2 km on the abyssal plain (CMP 1400) to 4 km at the base of the midslope terrace (CMP 3000) reflecting the initial sediment thickness variations of

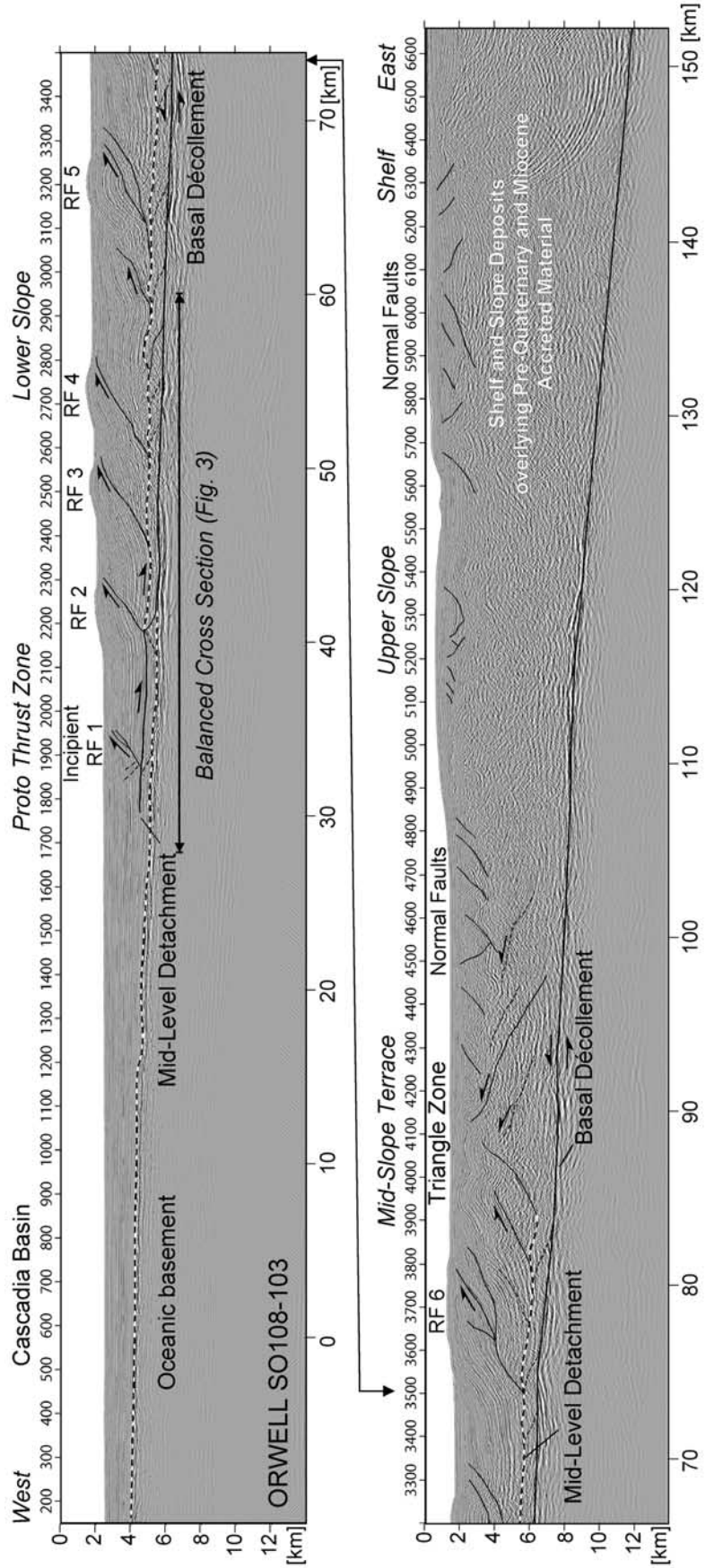

Figure 2. Structural overview of the accretionary wedge offshore Washington of the undeformed Cascadia Basin sediment succession and the accretionary prism east to the shelf as imaged in seismic profile SO108-103 (prestack depth migration, no vertical exaggeration). Observed and presumed thrust and normal faults are indicated by thin continuous and dashed lines. The active basal decollement and midlevel detachment (MLD) are indicated by a thick line. The inactive MLD is shown as a thick dashed line in the wedge. The heavy dashed line in the Cascadia Basin indicates the position of the proto-decollement, RF 1–6: ramp folds indicating position of backthrusts in frontal accretionary wedge.

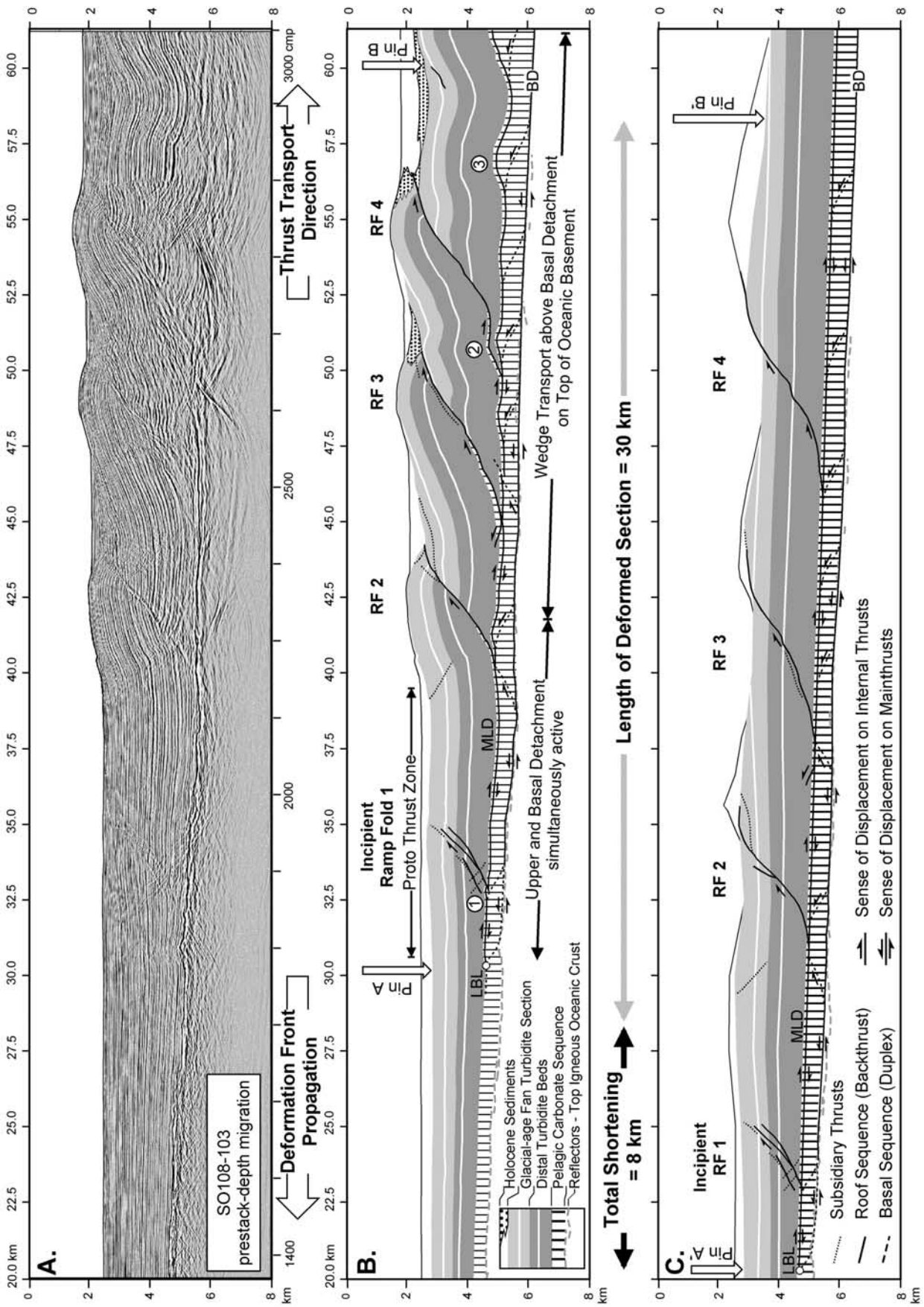
A.
SO108-103
prestack-depth migration
Deformation Front
Propagation
Thrust Transport
Direction
3000 cmp
B.
Incipient
Ramp Fold 1
Proto Thrust Zone
Pin A
Pin B
RF 2
RF 3
RF 4
LBL
MLD
BD
Upper and Basal Detachment
simultaneously active
Wedge Transport above Basal Detachment
on Top of Oceanic Basement
Holocene Sediments
Glacial-age Fan Turbidite Section
Distal Turbidite Beds
Pelagic Carbonate Sequence
Reflectors - Top Igneous Oceanic Crust
Total Shortening
= 8 km
Length of Deformed Section = 30 km
C.
Incipient
RF 1
Pin A'
Pin B'
Subsidiary Thrusts
Roof Sequence (Backthrust)
Basal Sequence (Duplex)
Sense of Displacement on Internal Thrusts
Sense of Displacement on Mainthrusts
km

Figure 3

the basin floor sediment succession and overlaying fan deposits prior to thrust stacking.

[18] Ongoing Quaternary to Holocene sedimentation in the Cascadia Basin and on the lower slope buried the bathymetric expression of the trench and most of the thrust-controlled relief of the frontal accretionary wedge. The frontal accretionary prism forms the shallow-inclined lower slope at the base of the continental margin with an average slope of the sea floor of about 2°. The oceanic basement is clearly imaged with an average eastward dip of 2° across the profile to a depth of about 7 km below sea level beneath the base of the mid-slope terrace.

[19] Seaward of the lower slope, the complete undeformed Cascadia basin succession with its thickened Quaternary sequence of the Nitinat Fan deposits (CMP 1400 to 2100) is imaged. The basinal succession is made of three sedimentary units, which can be clearly distinguished by their seismic velocities [*Flueh et al.*, 1998]. The lowermost unit rests directly on top of the oceanic basement and has been identified as a layer of pelagic calcareous deposits [*Duncan and Kulm*, 1989] characterized by significantly high velocities (up to 3.5 km/s) and minor thickness variations from 600 m to 800 m. The calcareous layer is overlain by a thick sequence of Pliocene/Pleistocene turbidite beds.

[20] The turbidite sequence can be divided in a lower section of distal silty turbidite current deposits with interbedded muddy units typical for the Cascadia abyssal plain [*Kulm et al.*, 1973, 1984] and an upper sequence consisting of very fine- to medium grained sandy turbidite beds of the Nitinat fan [*Applegate et al.*, 1992]. In the seismic section, the distal turbidite units are characterized by intermediate velocities (2.5 to 2.9 km/s) and continuously increasing thickness from 850 m (abyssal plain) to 1600 m (lower slope). The fan turbidite deposits show variations from intermediate (up to 2.5 km/s-lower member) to low velocities (2.2 km/s–upper member). Thickness variations of the fan turbidite deposits range from 850 m in the abyssal plain to at least 1100 m in the external thrust segment. Across the fold crests of the frontal accretionary prism the fan turbidite deposits are topped by an erosional discontinuity. In the abyssal plain and in structurally controlled thrust-top basins between adjacent ramp anticlines, the fan turbidite deposits are covered by up to 350 m thick Holocene sediment beds with low velocities (1.7–2.1 km/s).

[21] The MCS profile SO 108-103 images a complete fold train consisting of five widely spaced open ramp folds in the Quaternary frontal accretionary prism beneath the lower slope and one in an early stage of formation localized in the proto-thrust zone at the deformation front (Figure 2: RF1–RF6). The transition from the backthrust-dominated Quaternary accretionary wedge to the forethrust-dominated Pre-Quaternary and Miocene accretionary wedge is marked by a triangle zone beneath the mid-slope terrace. Remnants of seaward-vergent thrusts are imaged in the external Pre-Quaternary accretionary wedge landward of the triangle zone. Frequent normal faults in the upper part of the Pre-Quaternary accretionary wedge and in the overlaying slope and shelf deposits image widespread near surface extensional processes.

[22] The reprocessed section of the frontal accretion structures focuses on the four external ramp anticlines (Figures 3a and 3b: RF1–RF4) that are controlled by landward vergent thrust faults with an overall listric geometry. Most of the vertical thrust displacement, accommodated by the ramp anticlines, is not exhibited in the bathymetric relief of the lower slope, because the structural depressions between the thrust ridges are partly filled by syntectonic thrust-top sediment. Because the thrust faults are breaking through the sea floor, the associated ramp anticlines are thrust over their own syntectonically eroded debris and cause complex synsedimentary deformation structures in the adjacent thrust-top basins (Figures 3a and 3b).

[23] Active tectonic deformation extends in the proto-thrust zone up to 20 km seaward of the morphological front of the accretionary prism marked by the bathymetric ridge of RF 2 (Figure 3b). At the seaward limit of the proto-thrust zone the active deformation front is marked by the onset of diffuse deformation with increased tectonic thickening and incipient thrust formation in the incoming sedimentary succession (RF 1, Figure 3b). In the seismic section SO108-103, the propagating diffuse deformation front is extending 3 km seaward of the incipient ramp anticline, and traces the leading tip of the blind midlevel detachment (LBL in Figure 3b).

5. Depth-to-Detachment Analysis

[24] From structural interpretation based on an earlier processing stage, it has been suggested that the complete sedimentary succession is frontally accreted at the deformation front [*Flueh et al.*, 1998]. However, from the improved iterative prestack-depth migrated seismic section, a midlevel detachment (Figures 3b and 3c: MLD) in the lower part of the stratigraphic succession is identified by various structural indicators. Its stratigraphic level, detachment geometry and kinematics are confirmed by a depth-to-detachment analysis (Figure 4) and the constraints from balanced cross section construction.

[25] In the seismic section, the stratigraphic level of the midlevel detachment is indicated by the fault geometry of the incipient ramp fold in the proto-thrust zone (RF 1, Figures 3a and 3b). Here the developing backthrust and the conjugate forethrust shear zone merge in the stratigraphic level of the basal beds of the distal turbidite section

Figure 3. (a) Prestack depth migration of MCS line SO 108-103 (no vertical exaggeration). Detailed section of the proto-thrust zone, active deformation front and late Pleistocene to Holocene frontal accretionary structures (CMP 1400 to 3000). (b) Structural interpretation, fault kinematics, and balanced cross section of the frontal accretionary structures. (c) Restored section of the frontal and basal accretionary structures (deformed state A-B to restored state A′-B′) showing a total shortening of 8.5 km for the investigated 30 km long deformed section. MLD, midlevel detachment (roof thrust); BD, basal decollement (floor thrust); LBL, leading branch line (tip of blind MLD).

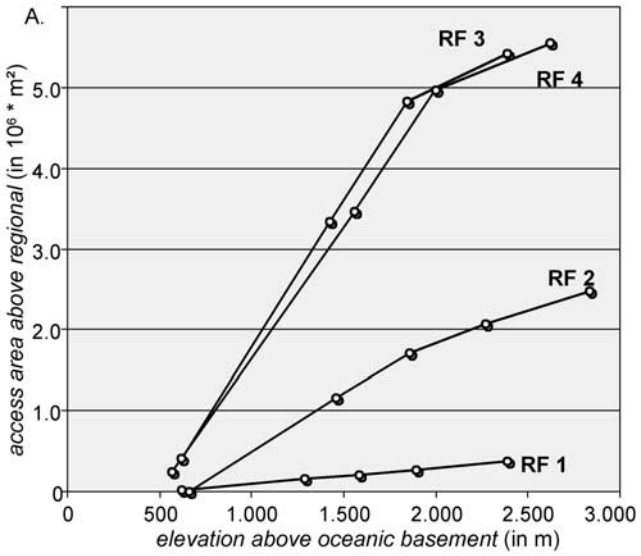

B.

seaward - landward	RF 1	RF 2	RF 3	RF 4
elevation of detachment above top oceanic crust	530 m	655 m	510 m	500 m
displacement on detachment	196 m	1428 m	3627 m	3304 m

Figure 4. Results of depth-to-detachment analysis of the seismic line SO 108-103. (a) Excess area graph; for each stratigraphic horizon the area tectonically uplifted above the initial stratigraphic level is plotted versus its initial elevation above the reference level, i.e., top oceanic basement. The elevation of the detachment above reference level is given by the intersection of the line with the x axis, and the displacement on the detachment is given by its slope. (b) Results of depth-to-detachment analysis.

(Figures 3a and 3b at marker position 1; Figure 5a). In the footwall of the fold structure, the underlying pelagic carbonate sequence directly overlying the igneous oceanic basement is not affected by faulting but is underthrust on top of the oceanic crust beneath the frontally accreted turbidite section.

[26] For structural balancing, the precise depth of the midlevel detachment is determined by depth-to-detachment analysis [*Epard and Groshong*, 1993] (Figure 4). The tectonically uplifted area (excess area) of individual stratigraphic levels in the ramp folds (RF 1–4) is used to obtain the best-fit values for the depth of the detachment and the thrust displacement along the accompanying flat-ramp segment assuming area conservation in the individual fold structures. The depth-to-detachment analysis validates the existence of the midlevel detachment within the uppermost level of the pelagic carbonate sequence with an average elevation of 500 m to 530 m above the top of the igneous oceanic basement (MLD in Figure 3b). Moderate depth variations are caused by initial sediment thickness variations of the pelagic carbonate sequence attributed to morphological variations of the igneous oceanic basement (Figure 3c) and tectonic thickening (for example, RF 2).

[27] The stratigraphic level of the passive roof thrust is located within the basal pelagic carbonate section, roughly 100 m below the stratigraphic contact with the distal turbidite beds and is not identical with the stratigraphic contact. For this stratigraphic level, no indications for significant mechanical variations are given by seismic velocities, porosity distribution and seismic attributes and thus an inherently mechanically weak layer is unlikely. We suggest that the localization of the detachment below the stratigraphic contact with the basal sequence of the silty distal turbidites with intercalated mud is controlled by overpressuring attributed to sedimentary loading. The mud layers at the base of the turbidite beds may act as low-permeability sealing for fluid flow. This interpretation is in coincidence with similar observations in the Oregon part of the Cascadia margin [*MacKay*, 1995].

[28] The horizontal thrust displacement of the ramp anticlines forming the lower slope varies from 1400 m to 3600 m. The inner ramp folds (RF 3, 4) have accumulated a displacement of 3.3 to 3.6 km indicating the maximum total shortening of individual thrust segments that is caused by initial frontal accretion of sediment beds entering the deformation front (in-sequence faulting). The seaward thrust segments (RF 2, displacement about 1428 m) and the incipient one in the proto-thrust zone (RF 1, displacement about 200 m) are active and still growing.

[29] In addition, the estimates of the excess area of individual stratigraphic levels in the ramp folds (excess area) reveal that only the incipient ramp fold (RF 1) is unaffected by syntectonic surficial erosion, sedimentation and re-sedimentation as shown by the linear trend curve (in Figure 4). In contrast, the anticlinal crests of the older ramp anticlines (RF 3, 4) are affected by surface erosion as indicated by the abrupt slope decrease of trend curves due to erosional area loss of upper stratigraphic levels (in Figure 4). In addition, the slope break indicated in the upper levels of the recently developing external ramp fold (RF 2) indicates reduced sediment accumulation on top of the growing ramp fault. The detachment depth and the thrust displacement are calculated from stratigraphic levels that are unaffected by surficial erosion.

[30] Besides the midlevel detachment, additional structural indicators in the more landward thrust segments to the east give strong indications for the existence of an additional basal detachment on top of the oceanic basement. Gentle upright fold structures with wavelengths of 1 to 3 km and landward dipping reflectors are observable in the turbidite beds in the footwall of the thrust ramps and the hanging wall flat segments overlaying the basal detachment (RF 3–5, Figures 3a and 3b at marker positions 2 and 3; Figure 5b). Artificial velocity pull-ups from seismic processing under the anticlinal crests of ramp folds can be excluded because upwarping of the underlying top of the oceanic crust is not observable.

[31] Because in the folds in the trailing hanging wall flat segments (for example RF 5, Figure 3b, marker position 3; Figure 5b) characteristic structural features as seaward-vergent dip domains, basal hanging wall cut-offs and associated secondary fold structures in higher levels of the

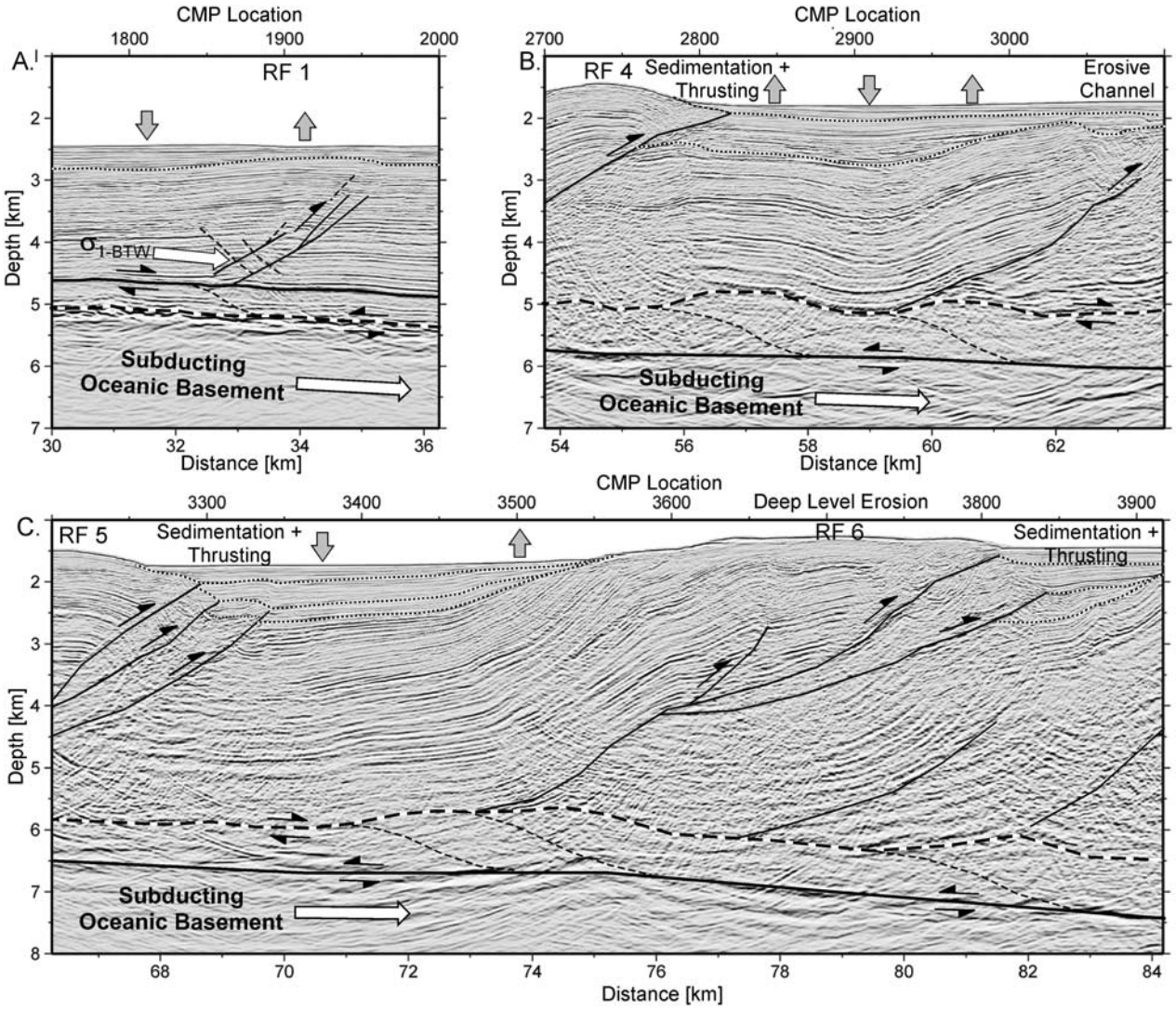

Figure 5. Seismic and structural details in the prestack-depth migrated seismic sections SO108-103: (a) Incipient ramp fold (RF 1) in proto-thrust zone, (b) passive folding of midlevel detachment by basal duplex formation, and (c) Synsedimentary deformation structures and growth strata on top of reactivated backthrust and associated ramp fold (RF 6). Thrust faults shown by narrow lines; the basal décollement is indicated by a thick line, the inactive MLD is shown as thick dashed line in the wedge. The dotted lines in the thrust-top basins indicate sedimentary discontinuities caused by tectonic movements. Shaded arrows indicate loci of structural uplift (tilted strata, onlap structures) and structural subsidence (growth strata).

ramp folds cannot be observed, ramp folding in the basal turbidite succession caused by a staircase fault geometry of the basal thrust ramp can be excluded. As consequence, the clearly imaged upright fold geometry in the structural position of the trailing hanging wall flat segment confirms that these structures were formed by passive folding of the footwall flat of the backthrusts.

[32] These structural observations confirm tectonic faulting and folding in the underthrust carbonate sequence in the footwall of the midlevel detachment. The syntectonic sedimentation in the structurally controlled thrust-top basins overlaying these fold structures (Figure 5b) and the absence of similar fold structures in the active seaward thrust segments indicate a later deformation after frontal accretion.

[33] Thus a more complex accretion mechanism with frontal accretion of the upper turbidite succession at the deformation front with simultaneous tectonic thickening and basal underplating of the basal carbonate beds beneath the seaward edge of the midslope terrace is imaged. The midlevel detachment at the top of the pelagic carbonate sequence enables frontal accretion of the turbidite succession and contemporaneous underthrusting and tectonic thickening of the pelagic carbonate sequence. The basal detachment on top of the oceanic basement decouples the

inner accretionary complex from the subducting oceanic crust and controls basal underplating of the underthrust pelagic carbonate sequence beneath the inner part of the frontal accretionary wedge sequence by duplex formation. Similar complex accretion mechanisms with frontal accretion and more landward basal underplating of parts of the sediment succession bypassing the deformation front were confirmed for other accretive margins, for example Alaska [*Ye et al.*, 1997]; Makran [*Platt et al.*, 1985]; and the Mediterranean Ridge [*Kukowski et al.*, 2002].

6. Diffuse Deformation in the Proto-Thrust Zone

[34] In addition to tectonic shortening estimated from the seismically imaged fault structures at many margins, a significant amount of tectonic strain is accumulated by diffuse deformation during frontal accretion of a sequence of trench sediment [*Bangs and Shipley*, 1999; *Morgan et al.*, 1995]. The processes and related deformation mechanisms were studied in detail in ODP cores. Tectonic thickening is attributed to pervasive small-scale brittle deformation by micro faults and deformation bands [*Karig and Lundberg*, 1990; *Maltman*, 1984; *Taira et al.*, 1992]. Ductile tectonic strain is indicated by arcward reduction of the porosity [*Bray and Karig*, 1988; *Taira et al.*, 1992].

[35] At Cascadia, in seismic profile SO108-103, diffuse deformation is evident from vertical thickening and arcward porosity loss in the basal pelagic carbonate oozes and the basal pre-fan turbidite beds (Figures 6a and 6b) and thus must be considered in quantitative strain estimates. The main part of diffuse deformation is accumulated in the seaward segment of the proto-thrust zone in the incoming sediment sequence bypassing the deformation front. The onset of arcward porosity reduction is imaged in the porosity distribution model seaward of the incipient ramp fold (km 30, CMP 1700, Figure 6a). A rather heterogeneous strain distribution is observable in the basal pelagic carbonate oozes and the immediately overlying distal turbidite beds (between km 30 and km 35 in Figure 6a). Arcward porosity loss in the basal pelagic carbonate beds (~10%) is significantly higher than in the overlying distal turbidite beds (~3%) and negligible in the younger Quaternary fan turbidite section. Additional to the increase of sediment thickness in landward direction, as extrapolated from the undeformed Cascadia basin sediment deposits, a pronounced tectonic thickening of the strata in the proto-thrust zone is identified in the basal carbonate units (~6%), in the lower distal turbidite beds (~14%), and in the more proximal turbidite deposits of the Nitinat fan (~12%) (refer to Table 1).

[36] Total diffuse tectonic shortening by tectonic thickening and horizontal porosity reduction is calculated for the sediment bypassing the deformation front and the initial ramp fold (km 30 to 35 in Figure 6a). Diffuse tectonic shortening is discontinuously accumulated in the lower part of the accreting stratigraphic succession and is significantly smaller in the basal distal turbidite beds (11%) than in the underlying carbonate section (15%) (Table 1). Diffuse strain is more effectively accumulated and propagates faster seaward in the carbonate section at the bottom of the accreted sequence than in the overlying terrigenous turbidite beds of the roof sequence.

[37] The excess diffuse tectonic shortening in the pelagic carbonate section ($\Delta \sim 210$ m) is balanced by an equal displacement along the midlevel detachment and on the incipient backthrust in the turbidite section of the roof sequence (displacement RF 1 $\sim$ 200 m). This down-section increase in excess shortening causes a shear sense reversal (top to arc) of the midlevel detachment that acts as a passive roof thrust (PRT) decoupling the turbidite section (roof sequence) from the underlying carbonate section (floor sequence) (illustrated by schematic strain ellipses in Figure 6a).

[38] The midlevel detachment (MLD = PRT) with its backthrust-sense mechanically decouples the passive roof sequence of distal turbidite beds and fan deposits that is still mechanically connected to the incoming Cascadia basin sediment succession from the underthrust basal carbonate section (floor sequence) and the basal décollement with top-to-sea shear sense (Figures 6b and 7).

[39] For this reason, the landward vergent backthrusts with their up-slope transport direction are the mechanically favored compressional structures in the passively transported turbidite beds of the roof sequence. Despite their uncommon observation in active accretionary prisms, the landward-verging thrusts should not be considered as atypical structures formed under extreme mechanical boundary conditions, but are controlled by the contrasting mechanical stratigraphy of the incoming sediment pile (see sections 9 and 10 for a more detailed discussion).

7. Structural Balancing of the Frontal Accretionary Wedge

[40] From the velocity/porosity model it is suggested that diffuse tectonic strain has been accumulated in the proto-thrust zone prior to the onset of the main thrust fault activity in the frontal accretionary wedge. Therefore the balanced structural cross section (Figure 3b) is constructed with respect to fault-related strain by line and area conservation in the already diffusely strained sediment succession bypassing the deformation front. As a consequence, the restored cross section (Figure 3c) does not consider diffuse deformation and sediment decompaction, bulk tectonic shortening e_{total} in the Quaternary accretionary wedge is

Figure 6. Diffuse deformation in the proto-thrust zone is mirrored through arcward porosity loss and tectonic thickening of the sediment. (a) Porosity distribution derived from seismic velocities. Discontinuous diffuse strain in the basal sediment is illustrated by strain ellipses obtained from strain analysis. (b) Detailed section of MCS line SO 108-103 (prestack depth migration, no vertical exaggeration) with fault kinematics and orientation of maximum principle stress along the midlevel detachment (MLD) and basal décollement (BD). LBL, leading branch line (tip of blind MLD).

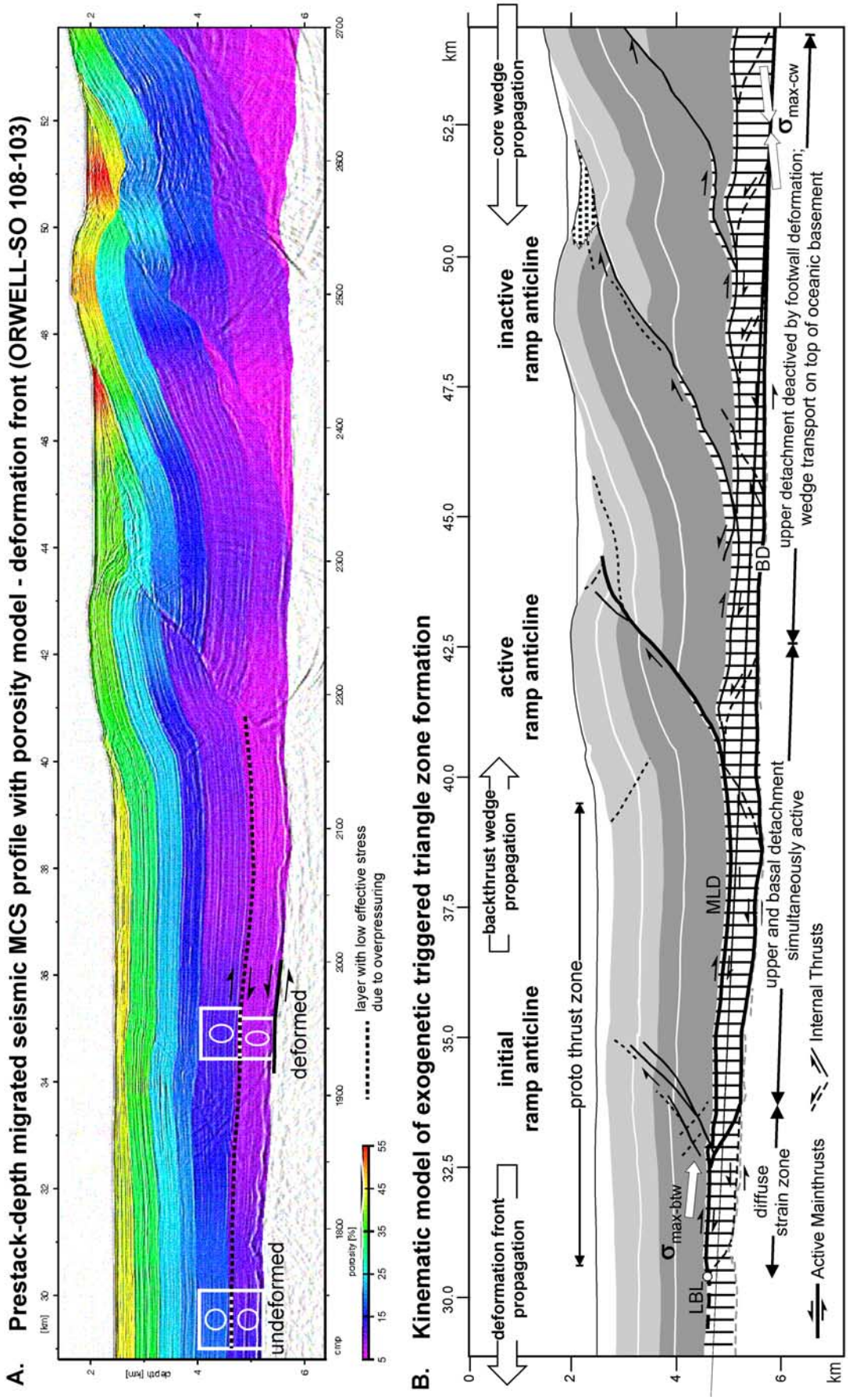
A. Prestack-depth migrated seismic MCS profile with porosity model - deformation front (ORWELL-SO 108-103)
undeformed
deformed
layer with low effective stress due to overpressuring
porosity [%]
B. Kinematic model of exogenetic triangle zone formation
deformation front propagation
initial ramp anticline
backthrust wedge propagation
active ramp anticline
core wedge propagation
inactive ramp anticline
proto thrust zone
σmax-btw
LBL
MLD
BD
diffuse strain zone
upper and basal detachment simultaneously active
upper detachment deactived by footwall deformation; wedge transport on top of oceanic basement
σmax-cw
Active Mainthrusts
Internal Thrusts
km

Figure 6

Table 1. Diffuse Tectonic Shortening in the External Proto-Thrust Zone (km 30–km 35) Deduced From Vertical Tectonic Thickening and Arcward Porosity Subduction of Sediment Beds

Stratigraphic Level	Porosity Loss, %	Initial Thickness or Thickness Variation	Deformed Thickness or Thickness Variation	Total Diffuse Tectonic Shortening, m
Upper Quaternary turbidites	negligible	14 m/10^{3}m	21.0 m/10^{3}m (12%)	430 (9%)
Lower pelagic turbidites	3	8.3 m/10^{3}m	20.3 m/10^{3}m (14%)	560 (11%)
Basal calcareous oozes	10	~590 (average)	~625 (average (6%))	770 (15%)

deduced from the fault-related strain e_{fault} and diffuse strain $e_{diffuse}$ (see section 8).

[41] In addition, layer parallel shear caused by heterogeneous diffuse deformation is mainly localized on the mid-level detachment in the proto-thrust zone. Significant layer-parallel shear is not expected to have been present in the ramp folds structures. Because of the clastic matrix of the turbidite beds, bending is accommodated by minor porosity change in the fold crest (for example, porosity change in RF 3, Figure 6a).

[42] The deformed structural section with a length of 30 km covers the frontal prism extending from the seaward edge of the proto-thrust zone (pin A in Figure 3b) up to the large thrust-top basin seaward of the broad mid-slope terrace (pin B located landward from RF 4 in Figure 3b). At the deformation front, only 80% of the incoming sediment succession, i.e., the entire turbidite sequence in the hanging wall of the roof thrust is frontally accreted forming imbricate thrusts with landward vergence. The major part of the basal carbonate section (20% of the incoming sediment succession, floor sequence) underthrusts the deformation front to a distance of at least 10 to 25 km beneath the frontal accretionary wedge where the basal section is detached from the oceanic basement and underplates beneath the inner thrust segments (RF 3–4).

[43] The landward vergent backthrusts as well as the basal duplex structures characterize the structural-controlled in-sequence deformation in the frontal imbrication zone characterizing the frontal and basal accretion of the Cascadia Basin sediment. Active deformation occurs in different structural positions. Initial diffuse deformation by tectonic shortening is active in the proto-thrust zone at the deformation front. Active shear deformation in the frontally accreted turbidite section is localized along the roof thrust, the backthrusts in the proto-thrust zone (RF 1) and beneath the leading ramp anticline (RF 2). In the basal sequence, active shear deformation occurs along the entire basal décollement and in the leading duplex faults beneath the inner ramp anticlines (RF 3, 4).

[44] The listric ramp geometry of the landward vergent thrusts is probably caused by the varying mechanical properties of the turbidite beds. The ramp angle is significantly smaller in the lower sequence of the distal turbidite section than in the upper distal turbidite and Quaternary fan turbidite beds. The active backthrusts (RF 1 and RF 2 in Figure 3b) are characterized by an average ramp angle of 36°–38°. The inactive faults (RF 3 and RF 4 in Figure 3b) still display listric shapes, but are characterized by a significantly flattened fault geometry with an average ramp angle of about 25° due to basal duplex formation and

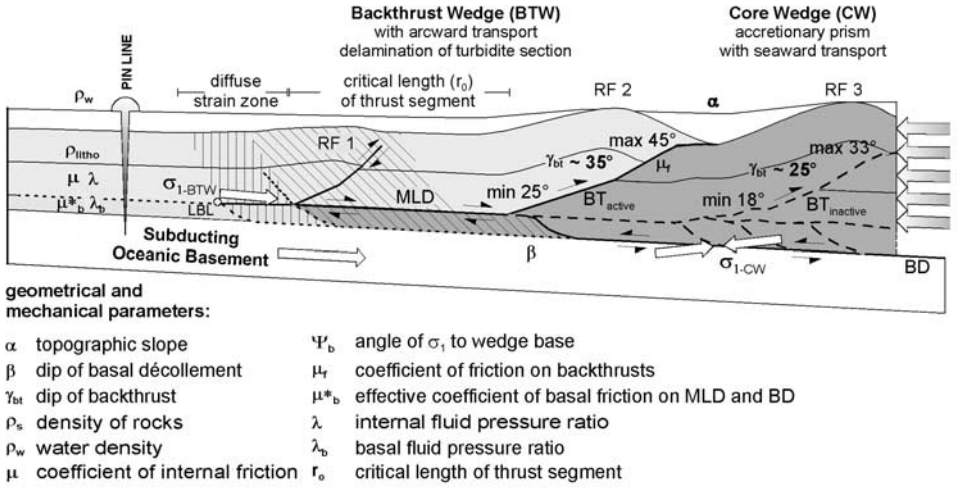

Figure 7. Kinematic features of the passive backthrust wedge and the core wedge composing the frontal accretionary prism with geometrical and mechanical parameters used for mechanical analysis. Hatched area indicates zone of diffuse deformation (with simultaneous fault deformation, oblique; without faulting, vertical); RF 1–3, outer ramp folds; MLD, midlevel detachment (roof thrust); BD, basal decollement (floor thrust); LBL, leading branch line (tip of blind MLD).

tectonic loading caused by the ramp anticline. Thrust spacing in the thick turbidite sequence (~2.5–3 km) involved in the upper imbricate thrust system is nearly constant (~8 km, length/thickness (l/t) ratio ~3), and varies moderately for the basal duplexes from 2.5 km to 4 km (l/t ratio 5–8). This uniform geometry of the thrust segments indicates stable mechanical conditions during frontal accretion and basal underplating.

[45] Structural interpretation of the complete profile SO108-103, that also images the entire continental slope, gives clear evidence for active out-of-sequence thrusting in the more landward part of the accretionary wedge (Figure 2, RF 6). Neotectonic to active out-of-sequence thrusting is caused by fault reactivation of an older backthrust beneath the innermost landward vergent ramp anticline at the seaward edge of the mid-slope terrace (Figure 5c). This fault separates the Quaternary frontal accretionary wedge from what we interpreted to be the triangle zone and the earlier Miocene accretionary complex beneath the midslope terrace and the upper slope that acts as a dynamic backstop of the frontal accretionary wedge.

[46] The deep erosion level at the crest of this large ramp anticline, characteristic synsedimentary deformation structures in the leading thrust-top basin, and growth strata in the trailing thrust-top basin indicate repeated thrust activity (Figure 5c). About 750 m of stratigraphic overburden was eroded from top of RF 6 which is nearly twice as much as observed in the innermost ramp anticline of the lower slope (RF 4 eroded sediment thickness ~400 m). In the trailing thrust-top basin, well-imaged onlap structures with several discontinuities reveal the episodic growth of the ramp anticline. Synsedimentary slump structures in the thrust-top basin at the tip of the thrust fault give evidence for Holocene fault activity. A minimum net displacement of 5 km is deduced from seismostratigraphic and structural considerations. This net displacement (equals in-sequence plus out-of-sequence thrusting) is accumulated by in-sequence displacement of about 3.5 km and by additional out-of-sequence thrusting due to fault reactivation of about 1.5 km.

8. Quantification of Quaternary Deformation

[47] Because of strain-partitioning in the accretionary wedge, Quaternary tectonic shortening of the frontal accretionary prism results from diffuse deformation of basin sediment in the proto-thrust zone ($e_{diffuse}$), and structural-controlled tectonic shortening (e_{fault}) by backthrusting beneath the lower slope (RF 1–RF 4) and fault reactivation of the older backthrust beneath the midslope terrace (RF 6).

[48] Restoration of the fault-related deformation in the 30 km wide frontal prism (pin line a - b in Figure 3b) results in a reconstructed section length of 38.5 km (pin line a′ - b′ in Figure 3c) and structural-controlled tectonic shortening of about 8.5 km (22%). Assuming additional diffuse tectonic shortening of the deformed sedimentary section of about 5–10%, the initial section length is estimated at 40.4 km to 42.4 km and total tectonic shortening ranges from 10.4 km to 12.4 km. Under consideration of additional tectonic shortening of about 1.5 km by fault reactivation in the mid-slope segment, total tectonic shortening ranges from a minimum of 12 km to maximum of 14 km in the frontal accretionary wedge.

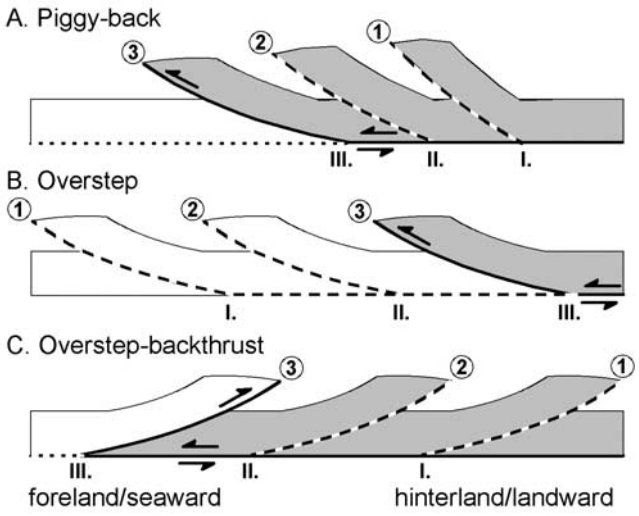

Figure 8. Schematic sketch illustrating basic thrust fault sequences in thrust belts and accretionary wedges and their implication for thrust transport, fault propagation, and deformation front migration. Fault sequence from 1 (old) to 3 (young); deformation front propagation from I (old) to III (young); active faults and detachment (bold lines); inactive thrust faults (dashed lines) and future detachment in basin/foreland sediment succession (dotted lines); actively propagating thrust/accretionary wedge (shaded areas).

[49] From this, the age of the frontal accretion structures and the rate of deformation front propagation can be estimated. Assuming a constant convergence rate of 42 mm/yr (~42 km/m.y.) between the Juan de Fuca plate and the North America plate in direction of the seismic section and continuous wedge growth, the frontal accretionary prism developed in the last 286,000 years (~12 km of convergence) to 333,000 years (~14 km of convergence). The net propagation of the active deformation front of 28.5 km in only 286,000 to 333,000 years results in a expeditious wedge growth rate of 8.6 to 10 cm/yr during the late Pleistocene and Holocene. This wedge growth rate exceeds previously published estimates obtained from microfossil assemblages of the lower slope anticlinal ridges by a factor of 6 [*Barnard*, 1973; *Carson*, 1977; *Silver*, 1972].

9. Fault Sequence, Wedge Kinematics, and Growth

[50] Commonly, in accretionary wedges and thrust belts, in-sequence thrusting occurs by forethrusts in piggyback sequence [*Boyer and Elliot*, 1982; *Butler*, 1982; *Elliott*, 1983] with the younger thrust formed in the undeformed footwall of the older thrust (footwall collapse by increasing tectonic load and raised pore pressure, Figure 8a). Inactive

forethrusts may be passively rotated and are transported in a piggyback manner by the younger one. When a new thrust segment becomes part of the thrust wedge, both, thrust transport and deformation front propagation are directed in the same direction (foreland indicates seaward). The counterpart mechanism was named overstep-sequence, where the new forethrust is initiated in the hanging wall of the active thrust [*Boyer and Elliot*, 1982; *Butler*, 1982; *Elliott*, 1983], and thrust transport and deformation front propagation are directed in the opposite direction (hinterland indicates landward; Figure 8b). However, an overstep forethrust sequence is unlikely because this would imply the hinterland migration of faulting in an already active thrust sheet.

[51] In contrast, backthrust formation is observed in an overstep-sequence in triangle zones or passive backthrust wedges in the foreland or frontal regions of mountain belts, in the case that the original definition given by *Butler* [1982] is focused on its primary kinematic feature, the relative structural position of younger and older thrust faults. Backthrust overstep-sequences were described from the Alberta foothills of the Canadian Cordillera [*Charlesworth et al.*, 1987], the Patagonia foothills of the Argentina Subandean thrust belt [*Ramos*, 1989], or the Kirthar and Sulaiman mountain belts of Pakistan [*Banks and Warburton*, 1986]. To avoid confusion with the original definition and its structural implications, we refer to the term ''overstep-backthrust sequence'' in this study (Figure 8c).

[52] The triangle zone and backthrust wedge formation are caused by differential tectonic shortening in a mechanically stratified sediment section with multiple detachment horizons (passive roof thrusting or passive roof duplexing), and is mainly observed at active mountain fronts, where the blind detachment is rapidly buried beneath young foredeep sediment. The structure, kinematics, and mechanical stability of this style of thrusting have been intensely investigated owing the high hydrocarbon potential of associated structures [*Banks and Warburton*, 1986; *Couzens and Wiltschko*, 1996; *Jamison*, 1993]. Until now, only ''onshore'' triangle zones and backthrust wedges have been investigated.

[53] Backthrust formation in the frontal Cascadia accretionary wedge off Washington also occurs in an overstep-backthrust sequence as deduced from the structural interpretation of the seismic profile SO108-103. Thrust formation in the hanging wall of the active thrust is initiated by increasing shear resistance of the active thrust fault due to increasing tectonic load, subsequent deformation or pore fluid drainage. This overstep-backthrust sequence is the kinematical key feature of the frontal accretionary prism. From these kinematic mechanisms to operate, two unique features are observed: (1) The directions of landward thrust transport and seaward propagation of the deformation front in the turbidite beds of the roof sequence are directly opposed. (2) The passively deforming thrust segment remains mechanically connected to the undeformed Cascadia Basin sedimentary sequence and is not part of the frontal accretionary wedge until the future seaward thrust is activated.

[54] The frontal accretionary prism is kinematically segmented into the passively deforming turbidite beds (backthrust wedge in Figure 7) and the actual accretionary wedge with seaward transport direction (core wedge). The seaward advance of the core wedge leads to a regional-scaled upward delamination of the basinal succession along the passive roof thrust, e.g., the midlevel detachment. The inner core wedge is bound by the active backthrust, the passive roof thrust and the basal décollement (Bt_{active}, RT, and BD in Figure 7). The initial triangle zone, that marks the transition from dominant seaward to landward vergent thrusts, is probably located beneath the mid-slope terrace (Figure 2). The backthrust wedge itself evolved after initial formation of the triangle zone. The backthrust wedge rests on the passive roof thrust with backthrust shear sense caused by progressive diffuse deformation in the basal floor sequence. The backthrust wedge is separated by the bounding backthrust from the inner core wedge. The deformation front marks the gradual transition into the undeformed Cascadia basin sedimentary sequence in a seaward direction.

[55] The seaward growth of the core wedge is controlled by the frontal accretion of successive backthrust wedge segments due to deactivation of the immediate landward backthrust and new fault formation in the seaward proto-thrust zone (overstep-backthrust sequence, Figure 7). The individual backthrusts became subsequently inactive because of duplex formation in the basal carbonate sequence and are transported on top of the duplexes as part of the in a seaward direction growing core wedge (for example, RF3 in Figure 7). Because of the complex fault kinematics, strain accumulation by initial fault formation and along active faults occurs in various structural positions. In the proto-thrust zone and the outer part of the lower slope (base of backthrust wedge: RF 1 and trailing part of RF 2), the active subduction interface is coincident with the roof thrust (RT in Figure 7; sectional length = 10 km). Beneath the more landward parts of the lower slope (base of core wedge: from the ramp segment of RF 2 to the east), the subduction interface steps down to the basal décollement on top of the oceanic basement (BD in Figure 7). Active deformation in the accretionary wedge focuses on the ramp segments of the two frontal anticlinal ridges (RF 1, RF 2 in Figure 7) and may episodically occur during fault reactivation along the ramp segment beneath RF 6 at the boundary to the mid-slope terrace (Figure 2).

[56] For modern subduction zones, the now identified offshore counterpart of continental triangle zones beneath the lower slope of the Washington accretionary prism is perhaps unique. However, in continental triangle zones the upward delamination of the roof sequence and tectonic shortening of the floor sequence are mostly caused by basal duplex formation. In contrast, the Cascadia backthrust wedge and the passive roof thrust (e.g., midlevel detachment) with backthrust shear sense are caused by progressive diffuse tectonic deformation in the basal floor sequence. Here, duplex formation is a second order feature characterizing late-stage basal accretion of the underthrust sediment beds of the floor sequence in a more internal position. Thus

duplex formation does not control the upward delamination process, but the mechanical locking of the internal imbricate thrust faults due to passive folding.

10. Backthrust Wedge and Core Wedge Mechanics

[57] To validate the kinematical concept of passive upward delamination of the backthrust wedge in front of the seaward propagating core wedge, both wedge segments need to obey the mechanical conditions required for the complex fault processes in the frontal accretionary prism. The propagation of the core wedge in a seaward direction requires a critical or stable dynamic state where the internal backthrusts are deactivated and the basal shear stresses reach or exceed the frictional strength of the basal décollement to allow basal transport without significant internal deformation. The delamination and passive overthrusting of the backthrust wedge onto the propagating core wedge is possible if the bounding backthrust is mechanically stable, e.g., in a mechanically favored position for active movement under the limiting stress conditions.

[58] To study the dynamic state of the frontal accretionary prism, we have analyzed the state of stress and the mechanical stability of the wedge-internal backthrusts and the décollement by the critical taper concept for friction-controlled convergent wedges [*Dahlen*, 1984; *Dahlen et al.*, 1984]. This concept was successfully applied to investigate the mechanics of accretionary wedges [see *Lallemand et al.*, 1994, and references therein] and the stability of continental backthrust wedges [*Jamison*, 1993]. The critical taper concept describes the relation between the wedge geometry, acting stresses, and the mechanical properties of the wedge. The deformation processes in the wedge are primarily controlled by its internal and basal friction coefficients (μ, μ_b) and pore pressure ratios (λ, λ_b). In addition to the internal and basal friction coefficients (μ, μ_b) considered in standard CT analysis, the taper and strength of friction-controlled deforming wedges are additionally controlled by the strength of active faults (μ_f) [*Lohrmann et al.*, 2003] as consequence of the strain hardening and softening properties of brittle rocks [*Byerlee*, 1978; *Mandl*, 1980; *Marone*, 1998].

[59] We show the graphical presentation with Mohr stress circles as proposed by *Lehner* [1986] to visualize the mathematical solution of [*Dahlen and Suppe*, 1988; *Davis and Dahlen*, 1983] for cohesive critical wedges (Figure 9) to model the mechanics of shallow deformation processes in sedimentary rocks, e.g., accretionary prisms and fold-and-thrust belts. Additionally to the dynamic wedge analysis, the Mohr stress circles give a graphical presentation of the critical state of stress as well as of the kinematics of the internal faults and the kinematics of the basal décollement in the backthrust and core wedges (Figures 9c and 9b). Using the pole construction method [*Lehner*, 1986; *Mandl*, 1988; *Terzaghi*, 1943] for the Mohr stress circle construction, the fault segments are plotted in the diagram with their actual dip angles (average, maximum and minimum fault dip γ as shown in Figures 7 and 9a) similar to the presentation in the seismic and structural profiles. Fault stresses are determined by the second intersection with the Mohr circle of any fault segment passing through the pole with its true dip in physical space.

10.1. Geometrical, Structural, and Mechanical Data Base

[60] For CT analysis, the geometrical data are derived from the seismic section (surface slope, basal dip). The structural fault parameters (max., min., and average dip angles of fault segments of the frontal backthrusts) are obtained from the depth-migrated high-resolution seismic section and are validated by structural modeling of the fault geometries from the fault-controlled fold geometries of sedimentary strata in the individual ramp folds.

[61] The physical properties (coefficient of internal friction, effective basal friction) are derived from the conjugate forethrust shear zone and the accompanied backthrust of the incipient ramp anticline (RF 1) in the proto-thrust zone using the method of *Davis and von Huene* [1987]. The obtained coefficient of internal friction, $\mu = 0.46$, is in the same range as in other accretionary wedges where a thick pile of sediment enters the subduction zone, e.g., Alaska, $\mu = 0.45$ [*Davis and von Huene*, 1987]; Nankai, $\mu = 0.50$ [*Lallemand et al.*, 1994], or Makran, $\mu = 0.42$ [*Kukowski et al.*, 2001]. For the backthrust wedge, the plunge of the axis of maximal principal stress ($\psi_b = 6°$) relative to the passive roof thrust is given by the bisector of the acute angle of the conjugate fault set. Additionally, the arcward dip of the σ_1 axis confirms the backthrust shear sense of the midlevel detachment (passive roof thrust) independently of the results from strain analysis (see Figures 6b and 7).

[62] The internal pore pressure ratio is assumed for a general submarine accretionary wedge without significant pore fluid overpressure with $\lambda = 0.6$ [*Lallemand et al.*, 1994]. Without wedge-internal overpressuring, the effective coefficient of basal friction along the midlevel detachment, deduced from μ and ψ_b, describes a moderately overpressured, weak detachment horizon ($\mu_b^* = 0.15$, $\lambda_b = 0.87$). We assume similar effective friction coefficients for the midlevel detachment and the basal décollement because the formation of the roof thrust is controlled by pore pressure that should not differ significantly between the top and base of the basal pelagic carbonate sequence owing to its small thickness. The reduced frictional strength of wedge-internal faults is conservatively assumed with $\mu_f = 0.42$ modeling sedimentary rocks with minor to moderate strain softening properties. The densities of the pore fluid ($\delta_w = 1030$ kg/m^3) and rock ($\delta_s = 2600$ kg/m^3) are assumed for seawater and sedimentary rocks. The cohesion gradient ($K = 2$ kPa/m) is characteristic for siliciclastic sediment beds in basinal environments with high sedimentation rates [*Dahlen and Suppe*, 1988; *Roeder*, 1992; *Zhao et al.*, 1986]. The complete geometrical, structural, and physical parameter set is summarized in Table 2.

10.2. Mohr Circle Construction

[63] For the mechanical analysis, the state of stress in the backthrust wedge is analyzed at the branch point of the

midlevel detachment and the bounding backthrust (RF 2), and similarly in the core wedge for the base of the landward backthrust (RF 3) (circles with (σ_n^*, τ) in Figure 9a). The corresponding gravitational state of stress (effective normal stress σ_n^* and shear stress τ, ($\sigma_n^*(z)$, $\tau(z)$) in Figures 9b and 9c) is limited by the overburden (D): D = 2600 m in the backthrust wedge, D = 3000 m in the core wedge), the internal pore pressure ratio (λ), and the effective surface slope α' [*Dahlen and Suppe*, 1988; *Davis and Dahlen*, 1983].

[64] The wedge-internal stresses are controlled by the strength of the rock and fault material (μ, μ_f). Maximum critical tectonic stresses and initial fault formation is controlled by the peak frictional strength of undeformed rock material described by the coefficient of internal friction (μ) and the depth-dependent cohesion ($C_0 = K \times z$). Therefore the limiting state of stress at the branch points in a depth z is controlled by the respective gravitational stresses ($\sigma_n^*(z)$, $\tau(z)$) and the critical shear strength of the wedge material ($\tau_{crit} = \pm(K \times z + \mu \times \sigma_z^*)$). It is represented by the Mohr stress circles in Figures 9a and 9b. In contrast, the faults are characterized by a significantly decreased frictional strength ($\tau_{fault} = \pm(\mu_f \times \sigma_z^*)$ with respect to that of the intact host rock enabling faults with variable dip to be active under critical stresses, horizontal hatched secants of Mohr circles in Figures 9b and 9c). Active faulting is possible along backthrusts when the shear stress on all fault segments exceeds the strength of the wedge-internal faults. Finally, the internal stresses in the accretionary prism are balanced by the basal shear stresses along the wedge base. The latter ones are controlled by the effective strength (μ_b^*) of the wedge décollement (core wedge) and the midlevel detachment (backthrust wedge) ($\tau_{base} = \pm(\mu_f \times \sigma_z^*)$ in Figure 9c).

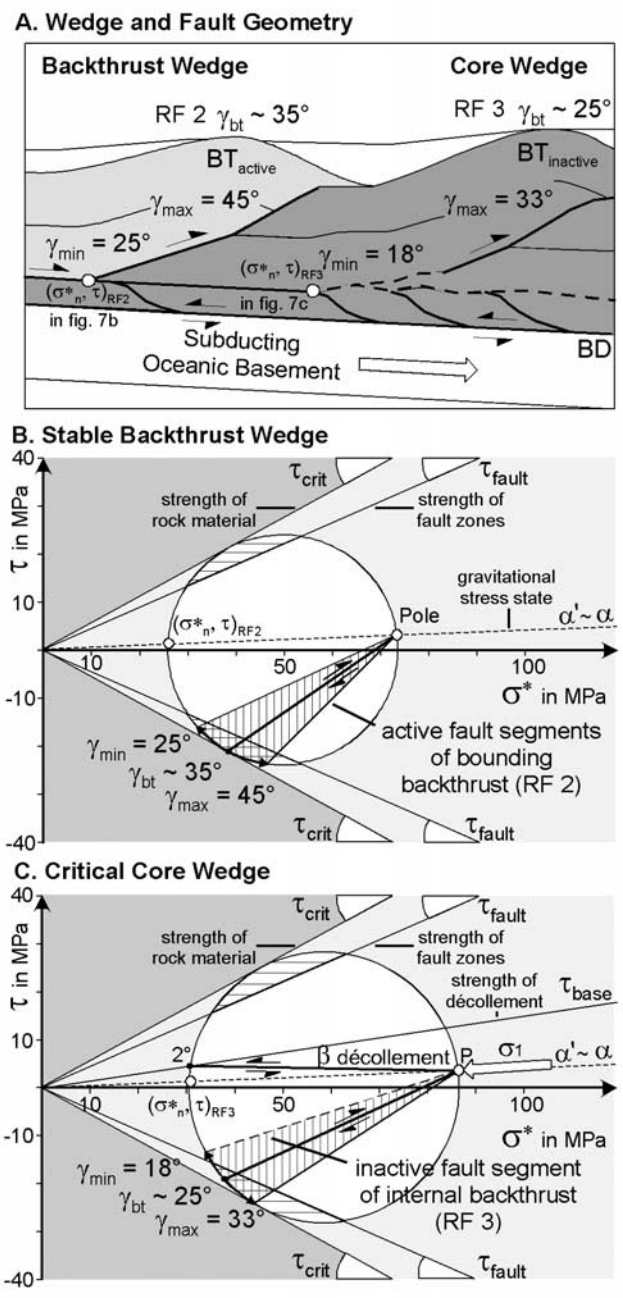

10.3. Backthrust Wedge Mechanics

[65] The taper of the backthrust wedge is defined by the surface slope and the dip of the bounding backthrust RF 2 (BT_{active} in Figures 7 and 9a). In the undeformed material of the backthrust wedge, initial failure under critical stress conditions is expected on backthrusts dipping seaward at

Figure 9. Graphical presentation of Critical Taper analysis for cohesive critical wedges of the frontal accretionary prism. Mohr stress circles show the graphical presentation of the critical state of stress and fault kinematics. In the stress diagrams the fault segments are plotted with their actual dip angles (average, maximum, and minimum fault dip γ as shown in Figure 9a) using the pole construction method. The limiting state of stress (stress circles) at the branch points is controlled by the gravitational stresses (σ_n^*, τ) and the critical shear strength of the wedge material (τ_{crit}). Faults are characterized by a significantly decreased frictional strength (τ_{fault}) enabling faults with variable dip to be active under critical stresses (horizontal hatched secants of Mohr circles). (a) Simplified presentation of the backthrust/core wedge geometry, dip variations of fault segments for backthrusts RF 2, RF 3, and reference points for the mechanical analysis (circles with (σ_n^*, τ)). Dashed fault segments are mechanically unstable. (b) State of stress in the stable backthrust wedge: Dip variations of ramp segments between 25° to 45° are observable (vertical hatched fault dips in Figure 9b). For all fault segments, the tectonic stresses exceed the fault strength (horizontal hatched secant of stress circle). (c) State of stress in the critical to stable core wedge: For the basal dip of $\beta \geq 2°$, basal shear stresses reach the décollement strength (τ_{base}, and line β décollement). The backthrust RF 3 (vertical hatched fault dips) became inactive, because shear stresses exceed the fault strength only on the steeper dipping ramp segments ($\gamma_{bt} > 20°$). On the flatter basal ramp segments ($\gamma_{min} = 18°$) the critical stress conditions are not matched (inactive fault segment).

Table 2. Geometrical Data, Structural Data, and Physical Properties Used in the Mechanical Analysis

Parameter	Value		Source
	Backthrust Wedge (BTW)	Core Wedge (CW)	
	Geometry Data		
Topographic slope (α), deg	0°–2°	2°	seismic line SO 108-103
Basal dip (β), deg	1.5° (midlevel detachment)	1.8° (basal décollement)	seismic line SO 108-103
Actual taper ($\alpha + \beta$), deg	1.5°–3.5°	3.8°	seismic line SO 108-103
	Structural Data Set		
Forethrust ramp angle (γ_{ft}), deg	RF1: 40°		seismic line SO 108-103
Backthrust ramp angle (γ_{bt}), deg	~35°; max. 45°, min. 25°	~26°; max. 33°, min. 18°	seismic line SO 108-103 + structural model
Critical length of thrust segment (r_0), km	~8 (imbricates)	2.5 to 4 (duplexes)	seismic line SO 108-103 + [*Dahlen et al.*, 1984]
	Mechanical Properties		
Density of rock (δ_{litho}), kg/m^3	2600		
Density of pore fluid (δ_w), kg/m^3	1030		
Cohesion ($C_0 = k \times z$; depth z)	k = 2 kPa/m (deformed sediments); C_0 = 4 to 6 MPa		typical values k = 1–5 kPa/m [*Zhao et al.*, 1986]
Coefficient of internal friction (μ)	0.46 (ϕ = 25°) peak friction of undeformed sediments		conjugate faults in PTZ [after *Davis and von Huene*, 1987]
Coefficient of friction on faults (μ_f)	0.42 (ϕ_f = 23°) reduced fault strength by strain softening		
dip of σ_1 direction to base (ψ_b), deg	6° arcward dip	5.5° seaward dip	conjugate faults (BTW); critical taper analysis (CW)
Effective coefficient of basal friction (μ_b^*)	0.15 (ϕ_b^* = 8.5°) effective strength of RT and BD		derived from ψ_b, μ [*Davis and von Huene*, 1987]
Internal pore fluid pressure ratio (λ)	0.6 (submarine wedge)		derived from μ_b^*, λ [*Dahlen*, 1984; equation 13]
Basal pore fluid pressure ratio (λ_b)	0.87 (moderately overpressured)		derived from μ_b^*, λ [*Dahlen*, 1984; equation 13]
	Kinematical and Mechanical Results		
Dynamic state of wedge	mechanically stable	critical, $(\alpha + \beta)_{crit}$ = 3.8°	mechanical analysis (BTW), critical taper modeling (CW)

35°, which is the average ramp angle in the backthrust wedge. Because of the listric fault geometry of the incipient backthrust (RF 1) and the bounding backthrust (RF 2), dip variations of individual ramp segments between 25° to 45° are observable (vertical hatched fault dips in Figure 9b). For all these fault segments, the tectonic stresses exceed the fault strength (horizontal hatched secant of stress circle in Figure 9b). All fault segments of the bounding backthrust RF 2 are therefore active and the backthrust wedge is mechanically stable. In this dynamic stable state the backthrust wedge can be passively upward delaminated and continuously overthrusted onto the seaward propagating core wedge.

10.4. Core Wedge Mechanics

[66] The taper of the core wedge is defined by the surface slope and the dip of the basal décollement (Figure 7) resulting in an average wedge taper of $(\alpha + \beta) = 3.8°$. In the core wedge the strength of the décollement is controlled by the effective basal coefficient of friction (represented by line $\tau_{base} = \mu_b^* \times \sigma_z^*$ in Figure 9c). For the measured basal dip of $\beta \geq 2°$, the basal shear stresses reach that of the décollement strength (line β decollement in Figure 9c). Additionally, this is confirmed by the analytical estimates of the critical taper. For a cohesive wedge under given mechanical conditions the critical taper is given by $(\alpha + \beta) = 2.75°$ indicating a dynamically stable wedge state [*Dahlen and Suppe*, 1988, equations 1–5]. Also in the case of a noncohesive wedge, that generally requires higher wedge tapers, the critical taper estimate with $(\alpha + \beta) = 3.96°$ characterizes at least a critical wedge state [*Dahlen et al.*, 1984, equations 1–3].

[67] As consequence of the mechanical stable backthrust wedge and the critical to stable core wedge geometry, the core wedge can be basally transported in seaward direction in the case that its internal backthrusts are deactivated. This is tested for the individual fault segments of the former backthrust beneath RF 3 (vertical hatched fault dips in Figure 9c). Here, active shear stress exceeds the fault strength only on the steeper dipping ramp segments ($\gamma_{bt} > 20°$), whereas on the flatter basal ramp segments ($\gamma_{min} = 18°$) passively folded by basal duplex formation, the critical stress condition is not matched (inactive fault segment in Figure 9c) and thus the entire backthrust became inactive.

10.5. Accretion Mechanics

[68] During seaward propagation, the critical to stable core wedge underthrusts the stable backthrust wedge along the active bounding backthrust and peels off the turbidite roof sequence along the midlevel detachment from the floor sequence consisting of the pelagic carbonate section (RF 2 and MLD in Figure 7). Active deformation is localized along the basal décollement of the critical core to stable wedge and the younger seaward bounding backthrust.

[69] As derived from the structural interpretation, simultaneous duplex formation in the basal pelagic carbonate sequence at the leading edge of the core wedge subsequently destabilizes the active bounding backthrust by flattening and folding of the basal ramp segments. This successive destabilization of the bounding backthrust governs the interaction between the passive backthrust wedge and the seaward propagating core wedge. The overstep-backthrust sequence of faulting due to the abundance of the active bounding backthrust in favor of fault initiation in the hanging wall is characteristic for unstable backthrust wedges [*Jamison*, 1993]. This process results in seaward stacking of a series of backthrust wedges, each of which have first satisfied and than failed the critical wedge limits.

[70] The similar length of the subsequently stacked backthrust segments (~8 km for imbricates = critical length of thrust segments, r_0) confirms the homogeneous mechanical conditions during formation of the glacial age frontal accretionary wedge. The critical length of the thrust segments in the passively upward delaminated backthrust wedge is controlled by the physical properties (μ, μ_b, λ, λ_b, C_0, δ_w) and the dip of the midlevel detachment (β). Here the structural estimates are validated by the analytical solution with $r_0 = 8.1$ km for an average cohesion $C_0 = 5$ MPa [*Dahlen et al.*, 1984, equation 25].

10.6. Activation of the Midlevel Detachment by Glacial Age Sediment Loading

[71] In the study area offshore Washington, the glacial age sediment succession accumulated in the large Nitinat and Astoria deep sea fans were rapidly deposited from the Frazier and Columbia River drainage system [*Applegate et al.*, 1992; *O'Connor and Baker*, 1992; *O'Connor et al.*, 1995]. Therefore we propose that the gravitational loading by rapid sedimentation and increased thickness of the terrigenous turbidite beds should drastically modify the lithostatic as well as the pore pressure in the buried Cascadia Basin sediment succession which enabled the activation of the midlevel detachment. From estimates of lithostatic and pore pressure in the Cascadia Basin sedimentary succession (Figure 10a) and their mechanical variation, we present a conceptional model for the activation of the midlevel detachment (passive roof thrust) in a regional scale as well as for the deformation processes in the frontal accretionary prism in the pre-Quaternary and glacial age to present time (Figures 10b and 10c).

[72] In pre-Quaternary time (Figure 10b), the sediment thickness of the incoming Cascadia Basin sedimentary succession was about half of the present thickness including the fan deposits. The depth variation of lithostatic and pore pressure in the sediment column entering the deformation front (Figure 10a) was calculated for hydrostatic conditions in the turbidite section ($\lambda = 0.6$) and for moderate overpressure in the basal pelagic carbonate section ($\lambda = 0.87$). Owing to minor loading caused by the distal turbidite beds only a small increase of pore pressure is observable across the potential midlevel detachment. Because the resulting effective stress drop causes no significant strength contrast along the formation boundary, the midlevel detachment cannot be activated (Figure 10b). Excess diffuse shortening in the basal carbonate section is accommodated by additional pervasive shear deformation in the basal part of the thrust segments. The complete sedimentary pile is frontally accreted above the basal décollement on top of the igneous

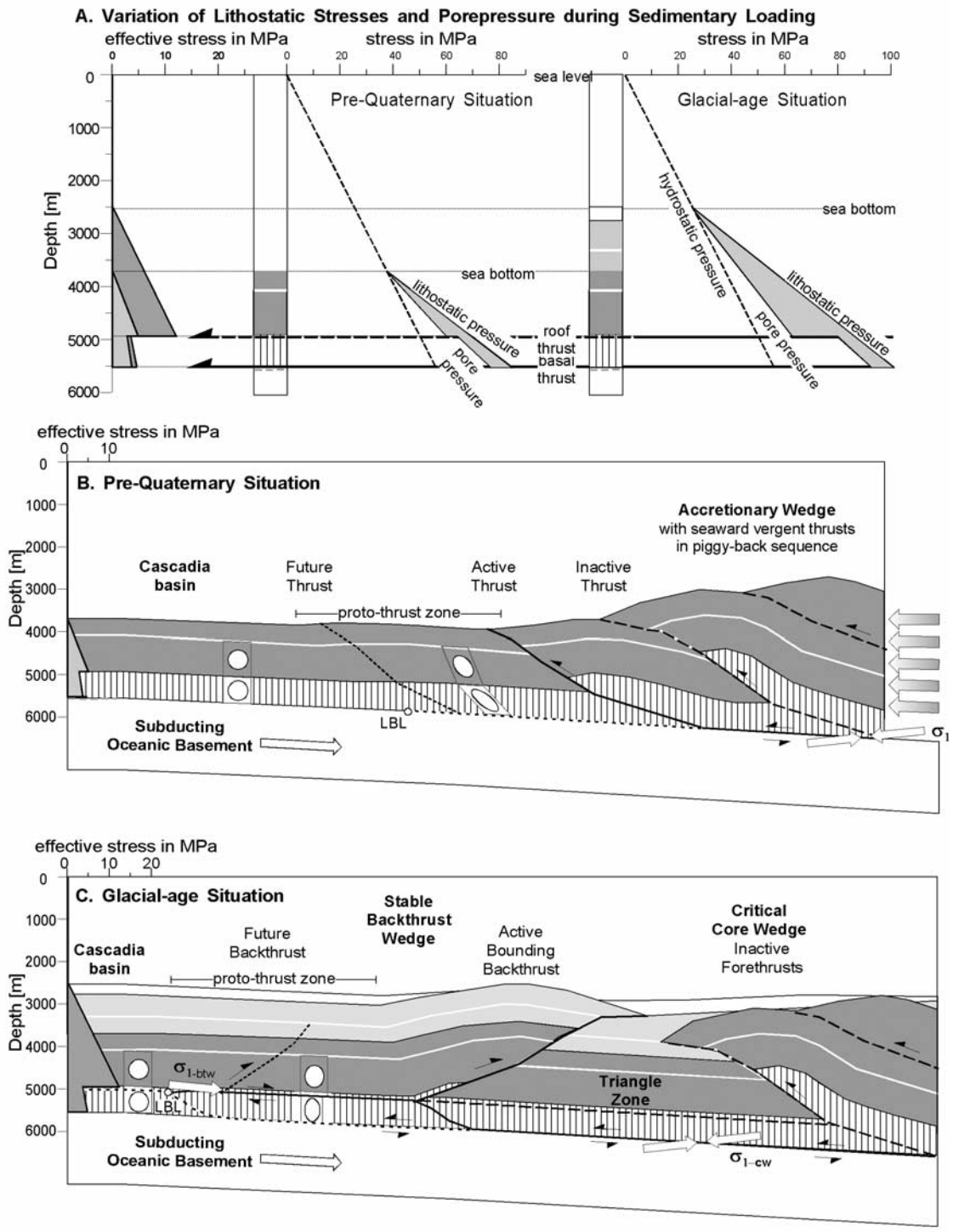

Figure 10. Dynamic model of the landward vergent backthrust formation in the frontal accretionary prism offshore Washington governed by the Quaternary sedimentation history. (a) Depth variation of lithostatic pressure, pore pressure and effective stresses in the Cascadia Basin sediment prior to and during Glacial age sediment loading. (b) Accretion of Cascadia Basin sediment by seaward verging forethrusts as consequence of the inactive roof thrust prior to the deposition of the Quaternary fan turbidite deposits. (c) Activation of the roof thrust by increased pore pressure due to gravitational loading by Quaternary fan turbidite deposits led to strain partitioning and passive backthrust wedging.

oceanic crust by seaward vergent thrusts. This is presently observable in the Vancouver and Southern Oregon segments of the accretionary wedge (Figure 1).

[73] The Glacial age situation differs significantly and is illustrated in (Figure 10c). As a consequence of the rapid deposition of the fan turbidite deposits gravitational loading by rapid deposition of the fan deposits drastically increased the lithostatic and pore pressure in the buried Cascadia Basin sediment succession. The overpressure in the basal pelagic carbonate section is significantly larger than in the overlying distal turbidites. This generates a strong effective stress drop and mechanical strength contrast across the potential midlevel detachment (Figure 10a). Excess shortening by diffuse deformation in the basal carbonate sequence caused strain partitioning and activation of the midlevel detachment as passive roof thrust with backthrust shear sense. This led to initial triangle zone formation and the generation of mechanically favored backthrusts (Figure 10c).

11. Discussion and Conclusions

[74] In this study, we have shown that the landward vergent thrusts beneath the lower slope of the Quaternary accretionary wedge offshore Washington are the structural expression of regional-scaled passive upward delamination of Cascadia Basin sediment succession in front of a seaward-propagating accretionary wedge. This accretion mechanism is controlled by the contrasting mechanical stratigraphy of the thick incoming sediment succession entering the subduction zone, and the formation of the midlevel detachment by gravitational loading caused by the rapid glacial age sedimentation of the Nitinat and Astoria fan deposits rather than by atypical mechanically boundary conditions in the frontal accretionary prism. This is the accretionary counterpart to triangle-zone and backthrust wedge formation at mountain fronts of continental fold-and-thrust belts.

[75] These unique characteristics of the frontal accretionary prism offshore Washington with their combination of a mechanical contrasting stratigraphy, and the dramatically increased sediment influx at the trench during the Pleistocene that triggers the activation of the potential midlevel detachment finally led to initial triangle zone formation and successive backthrust wedging. This combination of the mechanical potential and the exogenetic trigger for triangle zone formation and passive upward delamination seems rarely be established at other convergent margins. This may explain why other accretionary wedges, for example Alaska, Makran, southern Barbados Ridge, Hikurangi, and southern Chile, that are also characterized by a thick incoming sedimentary pile and rapid Quaternary sediment influx are dominated by seaward vergent thrusting.

[76] The regional delamination of Cascadia Basin sediment and seaward-stacking of backthrust wedges in front of the seaward propagating critical core wedge provides a kinematically and mechanically consistent model, that is confirmed by the quantitative structural model and strain data as well as the mechanical and frictional-wedge analysis. Solely with typical mechanical parameters for submarine accretionary wedges, mainly derived from structural interpretations, kinematical and mechanical analysis, the deformation processes can be explained by frictional-wedge mechanics and a Mohr-Coulomb rheological approach. The delamination process is dominantly controlled by heterogeneous diffuse deformation in the mechanically contrasting, basinal sedimentary succession, and strain partitioning along a midlevel detachment that was activated by localized overpressuring as consequence of rapid gravitational loading by the turbidite fan deposits. Therefore the deformation mechanism at the Cascadia convergent margin immediately responds to the strongly increased sediment flux. This reveals the short-term control of margin mechanics by rapid glacial age fan sedimentation.

[77] Our conceptional model does not need to invoke very low-basal friction [*MacKay*, 1995; *Seely*, 1977] or a viscous, non-Coulomb rheology in the basal part of the incoming sedimentary succession [*Gutscher et al.*, 2001], and thus it overcomes some problems still open in the previous mechanical concepts. The dip of the midlevel detachment (base of backthrust wedge) and the basal décollement vary only between 1.5° to 2° in the frontal accretionary wedge offshore Washington, and thus does not accomplish the requirement of significant arcward dip of the basal décollement in the very low basal friction model [*MacKay*, 1995]. For the observed subhorizontal dip of the wedge base additional seaward-directed thrusts and mixed structures with box-type folds should be expected [*Lallemand et al.*, 1994; *Mulugeta*, 1988].

[78] The complex deformation processes in the frontal accretionary wedge with dominant landward thrusting can be very well explained in terms of friction-controlled Coulomb wedge mechanics as often applied to accretionary wedges without the need of a viscoelastic basal layer in the incoming sediment pile. The backthrusts in the overlying sedimentary sequence show a structural and kinematical comparable behavior because they are caused in both cases by comparable mechanism: (1) diffuse strain by tectonic compaction and micro fracturing (Coulomb rheology, this study), and (2) ductile strain by cataclastic flow (viscoelastic rheology *Gutscher et al.* [2001]) by the differential distributed shortening and strain partitioning along a midlevel detachment. While the assumption of the more complex rheology with the basal viscoelastic layer is capable to explain the frontal landward vergent thrusts, it would lead to a mechanical inconsistency. In a viscoelastic layer with ductile behavior which is underthrust into greater depths beneath the frontal accretionary wedge, subsequent brittle faulting with duplex deformation as confirmed by high-resolution seismic imaging and structural modeling can not satisfactorily be explained because increasing temperature and pressure in the subducting layer should increase the potential for ductile deformation.

[79] Furthermore, our results concerning the complex fault kinematics and the distribution of active fault deformation in the frontal accretionary wedge may be of major importance in assessing the location of active faults and their seismic potential in the northern Washington segment of the Cascadia margin. Besides the deformation front and the basal décollement (e.g., subduction interface), active

deformation processes occur simultaneously in different parts of the accretionary wedge, namely in the landward part of the accretionary wedge by basal duplex formation and episodic out-of-sequence thrusting, and along the midlevel detachment beneath the proto-thrust zone. Because these faults are located within the seismic-locked zone, they may show an increased potential for seismic deformation. Of particular interest for risk assessment is the stratigraphically controlled midlevel detachment in the Cascadia Basin sediment succession. Because of its probable regional extend across a more than a 100 km wide segment along strike the Washington margin as supported by seismic data of the Orwell project [*Fisher et al.*, 1999; *Flueh et al.*, 1998] and temperatures higher than 125° [*Oleskevich et al.*, 1999] being within the range proposed for the seismogenic zone, the midlevel detachment forms a potentially large rupture area (up to 1000 km^2) with high tsunami risk. As a consequence of its similar strength and kinematical coupling, it should be considered that a seismic rupture of the arcward subduction interface may propagate into the seaward midlevel detachment. Thus our results concerning fault mechanics and localization of active faulting give additional constraints for the potential source location and focal mechanism of earthquake deformation processes offshore Washington, and thus they are of major importance for future seismic risk analysis concerning large subduction earthquakes at the Cascadia margin.

[80] **Acknowledgments.** The seismic data were acquired during the Orwell cruise (SO108) funded by the Federal Ministry for Research and Technology (BMBF) of Germany through grant 003G108A and the USGS Hazards program. This study was financially supported by the Deutsche Forschungsgemeinschaft (DASAC; grant KL 1242/1-1 and Leibniz programme). We gratefully thank Dave Scholl, Roland von Huene, and two anonymous reviewers for helpful reviews of this manuscript.

References

Applegate, T., C. Goldfinger, M. E. MacKay, L. D. Kulm, C. G. Fox, R. W. Embley, and P. J. Meis (1992), A left-lateral strike-slip fault seaward of the central Oregon convergent margin, *Tectonics*, *11*, 465–477.

Bangs, N. L. B., and T. H. Shipley (1999), Fluid accumulation and channeling along the northern Barbados Ridge decollement thrust, *J. Geophys. Res.*, *104*, 20,399–20,414.

Banks, C. J., and J. Warburton (1986), "Passive-roof" duplex geometry in the frontal structures of Kirthar and Sulaiman mountain belts, Pakistan, *J. Struct. Geol.*, *8*, 229–238.

Barnard, W. D. (1973), Late Pleistocene deformation of Cascadia Basin turbidites along Washington continental margin, *AAPG. Bull.*, *57*, 768–769.

Black, J. L., and M. A. Brzostowski (1994), Systematics of time-migration errors, *Geophysics*, *59*, 1419–1434.

Boyer, S. E., and D. Elliot (1982), Thrust systems, *AAPG. Bull*, *66*, 1196–1230.

Bray, J. C., and D. E. Karig (1988), Dewatering and extensional deformation of the Shikoku Basin hemipelagic sediments in the Nankai Trough, *Pure Appl. Geophys.*, *128*, 725–747.

Butler, R. W. H. (1982), The terminology of structures in thrust belts, *J. Struct. Geol.*, *4*, 239–245.

Byerlee, J. (1978), Friction of rocks, *Pure Appl. Geophys.*, *116*, 615–626.

Byrne, D. E., W. H. Wang, and D. Davis (1993), Mechanical role of backstops in the growth of forearcs, *Tectonics*, *12*, 123–144.

Byrne, T., and J. Hibbard (1987), Landward vergence in accretionary prisms: The role of the backstop and thermal history, *Geology*, *15*, 1163–1167.

Calvert, A. J. (1996), Seismic reflection constraints on imbrication and underplating of the northern Cascadia convergent margin, *Can. J. Earth Sci.*, *33*, 1294–1307.

Carson, B. (1977), Tectonically induced deformation of deep-sea sediments off Washington and northern Oregon: Mechanical consolidation, *Mar. Geol.*, *24*, 289–307.

Charlesworth, H. K. A., S. T. Johnston, and L. G. Gagnon (1987), Evolution of the triangle zone in the Rocky Mountain Foothills near Coalspur, central Alberta, *Can. J. Earth Sci.*, *24*, 1668–1678.

Clague, J. (1997), Evidence for large earthquakes at the Cascadia subduction zone, *Rev. Geophys.*, *35*, 439–460.

Couzens, B. A., and D. V. Wiltschko (1996), The control of mechanical stratigraphy on the formation of triangle zones, *Bull. Can. Pet. Geol.*, *44*, 165–179.

Dahlen, F. A. (1984), Noncohesive critical Coulomb wedges: An exact solution, *J. Geophys. Res.*, *89*, 10,125–10,133.

Dahlen, F. A., and J. Suppe (1988), Mechanics, growth, and erosion of mountain belts, *Spec. Pap. Geol. Soc. Am.*, *218*, 161–178.

Dahlen, F. A., J. Suppe, and D. Davis (1984), Mechanics of fold-and-thrust belts and accretionary wedges: Cohesive Coulomb theory, *J. Geophys. Res.*, *89*, 10,087–10,101.

Davis, D., and J. S. F. A. Dahlen (1983), Mechanics of fold-and-thrust belts and accretionary wedges, *J. Geophys. Res.*, *88*, 1153–1172.

Davis, D., and R. von Huene (1987), Inferences on sediment strength and fault friction from structures at the Aleutian Trench, *Geology*, *15*, 517–522.

Davis, E. E., and R. D. Hyndman (1989), Accretion and Recent deformation of sediments along the northern Cascadia subduction zone, *Geol. Soc. Am. Bull.*, *101*, 1465–1480.

DeMets, C., R. G. Gordon, D. F. Argus, and S. Stein (1990), Current plate motions, *Geophys. J. Int.*, *101*, 425–478.

Duncan, R. A., and L. D. Kulm (1989), Plate tectonic evolution of the Cascades arc-subduction complex, in *The Eastern Pacific Ocean and Hawaii.*, edited by E. L. Winterer, D. M. Hussong, and R. W. Decker, pp. 413–438, Geol. Soc. of Am., Boulder, Colo.

Elliott, D. (1983), The construction of balanced cross sections, *J. Struct. Geol.*, *5*, 101.

Engebretson, D. C., A. Cox, and R. G. Gordon (1983), Relative motions between oceanic and continental plates in the Pacific Basin, in *Proceedings of the Circum-Pacific Terrane Conference, Stanford Univ. Publ.*, *Geol Sci. Ser.*, vol. 18, edited by D. G. Howell et al., pp. 80–82, Stanford Univ., Sch. of Earth Sci., Stanford, Calif.

Epard, J.-L., and R. H. Groshong (1993), Excess area and depth to detachment, *J. Struct. Geol.*, *77*, 1291–1302.

Fisher, M. A., E. R. Flueh, D. W. Scholl, T. Parsons, R. E. Wells, A. M. Trehu, U. ten Brink, and C. S. Weaver (1999), Geologic processes of accretion in the Cascadia subduction zone west of Washington State, *J. Geodyn.*, *27*, 277–288.

Flueh, E. R., J. Adam, D. Klaeschen, and N. Kukowski (1997), Structure and physical properties of the frontal part of the accretionary wedge off Washington, *Eos. Trans. AGU*, *78*(46), Fall Meet. Suppl., 716–717, AGU.

Flueh, E. R., et al. (1998), New seismic images of the Cascadia subduction zone from Cruise SO108; ORWELL, *Tectonophysics*, *293*, 69–84.

Guo, N., and S. Fagin (2002), Becoming effective velocity-model builders and depth imagers, part 2, The basics of velocity-model building, examples and discussions, *Leading Edge*, *21*, 1210–1216.

Gutscher, M.-A., D. Klaeschen, E. Flueh, and J. Malavielle (2001), Non-Coulomb wedges, wrong-way thrusting, and natural hazards in Cascadia, *Geology*, *29*, 379–382.

Hyndman, R. D., K. Wang, and M. Yamano (1995), Thermal constraints on the seismogenic portion of the southwestern Japan subduction thrust, *J. Geophys. Res.*, *100*, 15,373–15,392.

Jamison, W. R. (1993), Mechanical stability of the triangle zone: The backthrust wedge, *J. Geophys. Res.*, *98*, 20,015–20,030.

Karig, D. E., and N. Lundberg (1990), Deformation bands from the toe of the Nankai accretionary prism, *J. Geophys. Res.*, *95*, 9099–9109.

Khazaradze, G., A. Qamar, and H. Dragert (1999), Tectonic deformation in western Washington from continuous GPS measurements, *Geophys. Res. Lett.*, *26*, 3153–3156.

Kukowski, N., T. Schillhorn, K. Huhn, U. von Rad, S. Husen, and E. R. Flueh (2001), Morphotectonics and mechanics of the Central Makran accretionary wedge off Pakistan, *Mar. Geol.*, *173*, 1–19.

Kukowski, N., S. E. Lallemand, J. Malavieille, M. A. Gutscher, and T. J. Reston (2002), Mechanical decoupling and basal duplex formation observed in sandbox experiments with application to the Western Mediterranean Ridge accretionary complex, *Mar. Geol.*, *3068*, 1–13.

Kulm, L. V. D., et al. (1973), Site 174, *Initial Rep. Deep Sea Drill. Proj.*, *18*, 97–167.

Kulm, L. D., P. W. Louhere, and J. S. Peper (1984), Geology of continental margin and Cascadia Basin, in *Western North American Continental Margin and Adjacent Ocean Floor off Oregon and Washington*, edited by L. D. Kulm et al., 29 pp., Mar. Sci. Int., Woods Hole, Mass.

Lallemand, S. E., P. Schnuerle, and J. Malavieille (1994), Coulomb theory applied to accretionary and nonaccretionary wedges; possible causes for tectonic erosion and/or frontal accretion, *J. Geophys. Res.*, *99*, 12,033–12,055.

Lehner, F. K. (1986), Comments on noncohesive critical Coulomb wedges: An exact solution by F. A. Dahlen, *J. Geophys. Res.*, *91*, 793–796.

Lohrmann, J., N. Kukowski, J. Adam, and O. Oncken (2003), The impact of analogue material parameters on the geometry, kinematics, and dynamics of convergent sand wedges, *J. Struct. Geol.*, *25*, 1691–1711.

MacKay, M. E. (1995), Structural variation and landward vergence at the toe of Oregon accretionary prism, *Tectonics*, *14*, 1309–1320.

MacKay, M. E., G. F. Moore, D. Klaeschen, and R. von Huene (1995), The case against porosity change: Seismic velocity decrease at the toe of the Oregon accretionary prism, *Geology*, *23*, 827–830.

Maltman, A. (1984), On the term "soft-sediment deformation," *J. Struct. Geol.*, *6*, 589–592.

Mandl, G. (1988), *Mechanics of Tectonic Faulting: Models and Basic Concepts*, 407 pp., Elsevier Sci., New York.

Mandl, W. C. G. (1980), On the theory of growth faulting Part II (a): Genesis of the unit, *J. Pet. Geol.*, *3*, 209–236.

Marone, C. (1998), Laboratory-derived friction laws and their application to seismic faulting, *Annu. Rev. Earth. Planet. Sci.*, *26*, 643–696.

McNeill, L. C., K. A. Piper, C. Goldfinger, L. D. Kulm, and R. S. Yeats (1997), Listric normal faulting on the Cascadia continental margin, *J. Geophys. Res.*, *102*, 12,123–12,138.

Morgan, J. K., D. E. Karig, and A. Maniatty (1995), The estimation of diffuse strains in the toe of the western Nankai accretionary prism; a kinematic solution, *J. Geophys. Res.*, *99*, 7019–7032.

Mulugeta, G. (1988), Modelling the geometry of Coulomb thrust wedges, *J. Struct. Geol.*, *10*, 847–859.

Niem, A. R., N. S. MacLeod, P. D. Snavely Jr., D. Huggins, J. D. Fortier, H. J. Meyer, A. Seeling, and W. A. Niem (1992), Onshore and offshore geologic cross section, northern Oregon coast range to continental slope, 73 pp., Oreg. Dep. of Geol. and Miner. Ind., Portland, Oreg.

O'Connor, J. E., and V. R. Baker (1992), Magnitudes and implications of peak discharges from glacial Lake Missoula, *Geol. Soc. Am. Bull.*, *104*, 267–279.

O'Connor, J. E., R. B. Waitt, and D. A. Johnston (1995), Beyond the channeled scabland, Oregon, *Geology*, *57*, 51–60.

Oleskevich, D. A., R. D. Hyndman, and K. Wang (1999), The updip and downdip limits to great subduction earthquakes: Thermal and structural models of Cascadia, south Alaska, SW Japan, and Chile, *J. Geophys. Res.*, *104*, 14,965–14,991.

Platt, J. P., J. K. Leggett, J. Young, H. Raza, and S. Alam (1985), Large-scale sediment underplating in the Makran accretionary prism, southwest Pakistan, *Geology*, *13*, 507–511.

Ramos, V. R. (1989), Andean foothills structures in northern Magellanes Basin, Argentina, *AAPG Bull.*, *73, 887–903.*

Roeder, D. (1992), Thrusting and wedge growth, Southern Alps of Lombardia (Italy), *Tectonophysics*, *207, 199–243.*

Satake, K., K. Shimazaki, Y. Tsuji, and K. Ueda (1996), Time and size of a giant earthquake in Cascadia inferred from Japanese tsunami records of January 1700, *Nature*, *379*, 246–249.

Seely, D. R. (1977), The significance of landward vergence and oblique structural trends on trench inner slopes, in *Island Arcs, Deep Sea Trenches and Back-Arc Basins.*, *Maurice Ewing Ser.*, vol. 1, edited by M. Talwani and W. C. Pitman III, pp. 187–198, AGU, Washington, D. C.

Silver, E. A. (1972), Pleistocene tectonic accretion of the continental slope off Washington, *Mar Geol.*, *13*, 239–249.

Snavely, P. D., Jr. (1987), Tertiary geologic framework, neotectonics, and petroleum potential of the Oregon-Washington continental margin, in *Geology and Resource Potential of the Continental Margin of Western North America and Adjacent Ocean Basins—Beaufort Sea to Baja California*, *Earth Science Ser.*, vol. 6, edited by D. W. Scholl, A. Grantz, and J. G. Vedder, pp. 305–335, Circum-Pac. Counc. for Energy and Miner. Resour., Houston, Tex.

Storti, F., F. Salvini, and K. McClay (2000), Synchronous and velocity-partitioned thrusting and thrust polarity reversal in experimentally produced, doubly-vergent thrust wedges: Implications for natural orogens, *Tectonics*, *19*, 378–396.

Taira, A., et al. (1992), Sediment deformation and hydrogeology of the Nankai Trough accretionary prism: Synthesis of shipboard results of ODP Leg 131, *Earth Planet. Sci. Lett.*, *109*, 431–450.

Terzaghi, K. (1943), *Theoretical Soil Mechanics*, John Wiley, Hoboken, N. J.

von Huene, R., D. Klaeschen, M. A. Gutscher, and J. Fruehn (1998), Mass and fluid flux during accretion at the Alaskan margin, *Geol. Soc. Am. Bull.*, *110*, 468–482.

Ye, S., E. R. Flueh, D. Klaeschen, and R. von Huene (1997), Crustal structure along the EDGE transect beneath the Kodiak shelf off Alaska derived from OBH seismic refraction data, *Geophys. J. Int.*, *130*, 283–302.

Zhao, W.-L., D. Davis, F. A. Dahlen, and J. Suppe (1986), The origin of convex accretionary wedges: Evidence from Barbados, *J. Geophys. Res.*, *91*, 10,246–10,258.

J. Adam, Department of Earth Sciences, Dalhousie University, Halifax, Nova Scotia, Canada B3J 3J5. (j.adam@dal.ca)

E. Flueh and D. Klaeschen, GEOMAR, Forschungszentrum für Marine Geowissenschaften der Christian-Albrechts-Universität zu Kiel, Wischhofstr. 1-3, D-24148, Kiel, Germany.

N. Kukowski, GeoForschungsZentrum Potsdam, Telegrafenberg, D-14473, Potsdam, Germany.